ADVANCED FUNCTIONAL MATERIALS

Supporting Information

for *Adv. Funct. Mater.*, DOI: 10.1002/adfm.201905054

Supramolecular Self-Assembly of Nanoconfined Ionic Liquids for Fast Anisotropic Ion Transport

Tomy Cherian, Danilo Rosa Nunes, Thomas G. Dane, Johan Jacquemin, Ulla Vainio, Teemu T. T. Myllymäki, Jaakko V. I. Timonen, Nikolay Houbenov, Manuel Maréchal, Patrice Rannou, and Olli Ikkala**

Supporting Information

Supramolecular Self-Assembly of Nanoconfined Ionic Liquids for Fast Anisotropic Ion Transport

Tomy Cherian, Danilo Rosa Nunes, Thomas G. Dane, Johan Jacquemin, Ulla Vainio, Teemu Myllymäki, Jaakko V.I. Timonen, Nikolay Houbenov, Manuel Maréchal, Patrice Rannou[*]*, and Olli Ikkala*[*]

Supporting Methods

Supporting Notes

Supporting Figures S1-S28

Supporting References S1-13

Supporting Method 1: Nuclear magnetic resonance spectroscopy (NMR) [Figures S6-8]

The room temperature solution-state nuclear magnetic resonance (NMR) spectra (^{1}H and ^{13}C NMR) were recorded on a Bruker Avance 400 MHz spectrometer equipped with 5 mm probe operating at 400.13 and 100.62 MHz for ^{1}H and ^{13}C, respectively. The measurements were performed using deuterated chloroform ($CDCl_3$ 99.8 % atom D) or dimethyl sulfoxide (DMSO-d_6 99.96 % atom D) as the solvents. The concentrations of the samples were adjusted to *ca.* 15-25 mg·mL^{-1} for both ^{1}H NMR and ^{13}C NMR measurements. NMR spectra of all studied supramolecular complexes are shown in Supporting Figures S6-8.

Supporting Method 2: *Ab initio* and density functional theory (DFT) calculations in gas phase

The *ab initio* and DFT calculations were performed using the Turbomole 7.2 program package.[S1] Before the visualization of the optimized 3D structure using TmoleX (version 4.3.2), all structures were optimized in the gas phase, with a convergence criterion of 10^{-8} Hartree, using HF/6-311++G** level of theory followed by DFT calculations combining the Resolution of Identity (RI) approximation[S2-S3] using the B3LYP function with the def-TZVP basis set.[S4-S6]

Supporting Method 3: Differential scanning calorimetry (DSC) [Figures S12, S14-17]

DSC thermograms of supramolecular complexes were measured using Mettler Toledo DSC821e and TA Instruments Q2000. The samples (mass of *ca.* 5-10 mg weighted into an aluminum pan) were first cooled down to either -20 or -50 °C from RT and equilibrated. Then two heating-cooling cycles were carried out between the starting temperature of -20 or -50 °C and the final temperature of 200 °C at a scan rate of 10 °C·min^{-1} with an isothermal resting time of 3 minutes at 200 °C.

Supporting Method 4: Polarized optical microscopy (POM) [Figure S12]

Melting and clearing points as well as liquid crystalline (LC) phases were characterized with a customized POM platform consisting of a DMLM (Leica) microscope working both in transmission and reflection modes and equipped with a series of x2.5, x5, x10, x20, and x50 objectives, a KY-F75 (JVC) 3 CCD camera, a LTS350 (Linkam) hot-plate, a CI94 (Linkam) temperature controller, and a LNP (Linkam) cooling system. The neat C_x-IL and DiC_x-IL supramolecular ionic liquid crystals (mass of *ca.* 2-5 mg) were sandwiched

between a (bottom) glass plate and a top cover glass at the room temperature (*i.e.* 23 °C). They were first heated (scan rate 10 °C·min^{-1}) under N_2 till reaching their isotropic states and immediately cooled down 5·°C below their clearing temperatures (as determined by DSC) to avoid their chemical degradation. The POM imaging was then conducted during cooling scans, using customized (adjusted to each C_x-IL and DiC_x-IL supramolecular complex) cooling scan rate (of *ca.* 2.5 to 0.5 °C·min^{-1}) and appropriate annealing procedures to allow for the development of birefringent textures related to their mesomorphic behaviors and related properties (See Figure S11).

All surfactant self-assembled supramolecular ionic liquid crystals C_x-IL and DiC_x-IL initially displayed featureless black images under cross polarizers at temperatures lower by *ca.* 5·°C from their clearing temperatures, indicating homeotropically aligned smectic mesophase. Extensive trituration of the top cover glass with a tweezer was necessary to generate typical LC defects within the thin (*ca.* 5-10 micron thick) mesomorphic layers, revealing the birefringence of the mesophases displayed by this family of supramolecular ionic liquid crystals. First, the development of small size bâtonnets, focal-conic fan or mosaic homogeneously aligned textures separating from a black background were observed for the series of C_x-IL and DiC_x-IL supramolecular complexes. Annealing procedures and appropriate cooling scan rates were identified to allow the growth of large size and fully developed birefringent textures such as i) the colorful mosaic textures of DiC_6-IL recorded at 110 °C (see Figure S12f) or ii) the colorful focal-conic fan and permanently arced focal-conic fan textures (see Figure 2c) of DiC_9-IL imaged at 130 and 25 °C, respectively.

Supporting Method 5: Temperature-dependent small/wide angle X-ray scatterings (SAXS/WAXS) [Figures S12-17 and Figure S28]

Variable temperature SAXS/WAXS measurements were performed at ESRF (European Synchrotron Radiation Facility, Grenoble, France) on ID13, BM02-D2AM, and BM28 beamlines. Additional SAXS/WAXS characterizations were performed using an in-house X-ray diffusion/diffraction setup (IRIG/DEPHY/MEM/SGX, Grenoble, France). The complementary measurements using X-ray reflectivity (ESRF/BM28) and μ-focus grazing-incidence diffraction (ESRF/ID13) were performed to confirm the already obtained data. The experiments used to obtain the data showed in the main text and in this Supporting Information are described below.

Experiments at the ID13 micro-focus SAXS/WAXS beamline

The beam of photons, λ = 9.537 nm (E = 13 KeV), with a focal size of *ca.* 1 mm^2 resulted in flux densities of *ca.* a few 10^{10} photons·s^{-1}·μm^{-2}. Patterns were recorded on a DECTRIS EIGER 4M single photon counting detector (CCD pixel detector) with 2070 x 2167 pixels (75 x 75 μm^2 pixel size) at a rate up to 750 Hz. The sample-to-detector distance (SDD) was set to 390 mm giving an accessible q-range spanning from 0.2 to 30 nm^{-1}. Silver behenate (AgBe, CAS number: [2489-05-6]) was used for the q-range calibration of the 2D detector. The measuring time for the X-ray scattering experiments was fixed to 2 s (with 1 ms resolution) in order to minimize the risk of radiation damage. The software package developed at ESRF was used for data reduction and to convert the 2D SAXS images to 1D SAXS profiles of radially averaged scattered intensity $I(q)$ *vs.* scattering-vector modulus q. Background contributions have been taken into account in the peak fitting procedure. Before further analysis, X-ray data were compensated for intensity fluctuations of the incoming X-ray beam.

Experiments at the BM02-D2AM SAXS/WAXS beamline

The incident photon energy was set to 24 keV, *i.e.*, corresponding to a wavelength of λ = 0.057 nm. Two 2D detectors were used. A CDD camera developed by Princeton (presently Ropper Scientific) for the SAXS acquisitions, and a silicon hybrid pixel detector from imXPAD, a WOS (WAXS Open for SAXS) allowing simultaneous acquisitions of X-ray diffraction (XRD) data covering SAXS and WAXS q-range. The scattering-vector modulus is defined as $q = (4\pi/\lambda)\cdot\sin\theta$, where θ is half of the scattering angle and λ is the wavelength. Two sample-to-detector distances (SDD) were used to cover two scattering-vector modulus q from 0.15 to 5 nm^{-1} (SAXS with SDD = 113 cm) and from 13 to 75 nm^{-1} (WAXS with SDD = 8 cm). The corrections of primary data were carried out using the software Bm2Img available on the beamline: **i)** the dark current (*i.e.* non-illuminated camera), **ii)** the flat-field response (*i.e.* homogeneously illuminated camera), and **iii)** the tapper distortion. Silver behenate (AgBe, CAS number: [2489-05-6]) and lanthanum hexaboride (LaB_6, CAS Number [12008-21-8]) were used as standards for the SAXS and WAXS q-range calibration, respectively. 2D images were converted into 1D radial averages over the image centre to yield the scattered intensity $I(q)$ *vs.* the scattering-vector modulus q. Complexes were sealed in home-made (copper brass-based) circular holders equipped with Kapton® windows. The contribution of

the empty cell was subtracted from the scattering intensity of the studied supramolecular complexes.

Experiments using a home-made SAXS/WAXS setup at CEA-Grenoble/IRIG/DEPHY/MEM/SGX

Variable temperature SAXS measurements were performed using a home-made (CEA-Grenoble/IRIG/DEPHY/MEM/SGX) SAXS line consisting in a FR591-3kW rotating anode (Nonius) with Cu K_α radiation, a set of two Ni-filtered focusing mirrors (Xenocs), and a VÅNTEC-2000 2D detector (Bruker). The incident photon energy was adjusted to 8 keV, *i.e.*, a wavelength of λ = 0.15118 nm. The sample-to-detector distance was set to 28 cm for covering a *ca.* 0.2 to 13.4 nm^{-1} angular range. The 2D detector was off-centred to increase the *q*-range for the anisotropic samples. Silver behenate (AgBe, CAS number: [2489-05-6]) was used for the *q*-range calibration of the 2D detector. The complexes were sealed in home-made (copper brass-based) circular holders equipped with Kapton® windows. Standard correction procedures were applied to the data for the background subtraction and normalization. The contribution of the empty cell was subtracted from the scattering intensity of the studied samples. 2D images were converted into radial averages over the image center to yield the scattered intensity $I(q)$ *vs.* scattering-vector modulus q using the Datasqueeze software. The intensity curves were scaled to the absolute intensities with the aid of a laboratory-calibrated Lupolen® sample. For temperature-resolved measurements, samples were subjected to a heating/cooling rate of 1.5 °C·min^{-1} and equilibrated for 4 minutes at each temperature before data acquisition.

Complementary room temperature WAXD measurements were also performed with a Rigaku SmartLab X-ray diffractometer (Aalto, OtaNano) with a rotating anode X-ray source (9 kW, Cu $K_{\alpha,\beta}$) and a 2D single photon counting pixel detector HyPix-3000 to complete and confirm the results.

Scherrer equation for crystallite size determination[S7] was adapted to extract the correlation lengths of the supramolecular complexes DiC_x-IL and C_x-IL. This reflects the long-range order present in these ionic conductors. Correlation lengths along the two axes *a* (perpendicular to ionic layers) and *c* (parallel to ionic layers) of the unit cells (see Figure 2 in the main text) were separately extracted as a function of the temperature. The following equation, adapted from the general Scherrer equation, was used to extract these values:

$$Correlation\ Length\ (nm) = \frac{K \cdot 2\pi}{\Delta q}$$

K = 0.9, dimensionless shape factor,

Δq = full width at half maximum of the peak in nm^{-1} ($q = (4\pi/\lambda)\cdot\sin\theta$, where 2θ is the scattering angle).

Supporting Method 6: Fourier-transform infrared spectroscopy (FTIR) [Figure S18]

The FTIR-spectra were measured on a Nicolet 380 spectrometer (Thermo Fisher Scientific) operating in the transmission mode in the 4000 - 400 cm^{-1} range with a 2 cm^{-1} resolution and averaged over 64 scans. The room temperature FTIR spectra of all supramolecular complexes are shown in Figure S18. The absorption peaks at 3274 and 3285 cm^{-1} of DiC_9-IL (See Figure S18b) are assigned to the stretching vibration of N-H bond in the secondary amine (for FTIR-spectra assignments, see Supporting reference[S8]). The peaks at 1565 cm^{-1} and 1573 cm^{-1} of DiC_9-IL (See Figure S18b) are assigned to the bending vibrations of the protonated secondary amino groups of (NH_2^+)[S8]. The peak at 1163 cm^{-1} in IL (See Figure S18b) is assigned to the stretching vibration of individual S=O bonds of the sulfonyl group. The peak at 1172 cm^{-1} of DiC_9-IL is assigned to the stretching vibration of SO_3^- group of the sulfonate formed in the supramolecular complex DiC_9-IL[S8]. The presence of the absorption peaks corresponding to the protonated amine and sulfonate groups in DiC_9-IL confirms the formation of the ionic complex. Other ionically self-assembled supramolecular ionic liquid crystals with double and single *n*-alkyl tails also show the characteristic absorption peaks of protonated amine and sulfonate groups (See Figures S18c-d).

Supporting Method 7: Electrochemical impedance spectroscopy (EIS) [See Figs S1-5, S11, S19-24 and S26]

The Electrochemical Impedance Spectroscopy (EIS) characterization of each supramolecular complex were carried out using an HF2IS Impedance Spectroscope equipped with an HF2IS-UHS (Ultra-High Stability) option and an HF2TA Current Amplifier. The impedance diagrams were recorded between 5 Hz and 10 MHz with an AC excitation of 100 mV.

The variation of the impedance is due to the rotational fluctuations of molecular dipoles in the studied supramolecular complexes. These dipoles are related to characteristic sub-parts of the molecules forming the supramolecular complexes or to the supramolecular complexes as a whole. As a consequence, their mobilities depend upon the local restrictions

imposed by their immediate surroundings. Upon an increase of the temperature, the dielectric constant usually decreases. This evolution is due to the dispersion of the dipole orientations coupled with an increase of the Brownian movements.

Parallel ion transport (along the ionic layers *i.e.* along *c* axis of the unit cell defined in Figure 2) in the main text was measured using liquid crystalline (LC) cells (Instec Inc.) with interdigitated in-plane ITO electrodes on glass substrate (denoted here as "parallel cells", see Figure 3a in the main text). Perpendicular ion transport (across the ionic layers, *i.e.* along *a* axis of the unit cell defined in Figure 2) was measured using LC cells (Instec Inc.) containing parallel ITO electrodes (sandwich configuration) on glass substrates (denoted here as "perpendicular cells", see Figure 3b in the main text).

Ionic conductivity was calculated using the following formula: σ_{ionic} [S·cm^{-1}] = K/R

K(cm^{-1}): cell constant of the parallel and perpendicular LC cells,

R: bulk resistance R_{bulk}(Ω) extracted from the impedance diagrams. The fitting procedure is demonstrated using selected examples in Figure S5. For additional background and reference procedures, see Supporting References[S9-S13].

K = 0.213 cm^{-1} and K = 0.0004 cm^{-1} for parallel and perpendicular LC cells, respectively. These cell constants were calculated using the geometry of the ITO electrodes in the cells. The LC cells were calibrated for each condition, *i.e.* each range of conductivity at each temperature (step of 10 °C over the 10-150 °C temperature range), to prevent measurements artefacts. The ionic liquid 1-decyl-3-methylimidazolium bis[(trifluoromethyl)sulfonyl]imide (IoLiTec, Ref IL-0100-HP, CAS Number [433337-23-6], Purity > 98 %) was used to evaluate the impedance of the set-up, mainly consisting of the impedance of the ITO electrodes, and to verify the cell constants.

Supporting Method 8: Thermogravimetric analysis (TGA) [Figure S25]

TGA analyses were carried out using TGA Q500 at a heating rate was 10 °C·min^{-1} using nitrogen as the carrier gas.

Supporting Notes

Supporting Note 1: Analysis of the ion transport measurements

The impedance data were fitted with *a priori* defined phenomenological models. A parallel circuit with a resistance and a constant phase element (CPE) is an adequate model for an electrolyte between (ionically) blocking electrodes[S10]. The first one represents the

dissipative contributions of the dielectric response, while the second describes the ability of the dielectric component to store the electric field through polarization mechanisms.

The CPE1 is used when a frequency dispersion of an electrical double layer originating from surface disorder, or a porosity/inhomogeneity of material surface, is assumed. The impedance of this non-intuitive circuit element is $Z(\omega)=1/(jC\omega)^n$, n being a fractional power (n = 0 to 1).

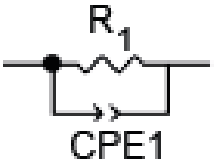

Figure S1. The Cole element

The related impedance with a resistance R_1 in parallel, so-called Cole element (see Figure S1), is represented in an electrochemistry Nyquist plot by an impedance diagram starting at high/medium frequencies by a depressed semi-circle (α is the angle of depression). A mesoscopic characteristic time $\tau = RC$ can be calculated and defined as the diffusion time at the mesoscopic scale in the complexes between 10 μs and 10 ms.

For DiC_X-IL supramolecular complexes (See Figures S4d-f), a heterogeneous electrolyte is assumed to take into account the polycrystallinity. In series, a remaining resistance for the setup, essentially the resistance of the ITO electrodes, with a Cole element for the DiC_X-IL-based electrolytes themselves was used. The capacitances and n were extracted by fitting. The capacitances in both parallel and perpendicular geometries were compared, for EIS measurements performed during "fast" *vs.* "slow" cooling, *i.e.* at 5 °C·min^{-1} and 0.5 °C·min^{-1} cooling rates, respectively.

Except for the EIS measurements in the parallel configuration up to 150 °C with a fast scan rate, capacitance (See Figure S2) values remain in the same order of magnitude. On one hand in the perpendicular configuration, the capacitance does not depend on the scan rate since the ionic transport is slow. On the other hand, capacitance values extracted from EIS measurements performed in the parallel geometry are lower when using a fast scanning rate as the polarization is less important.

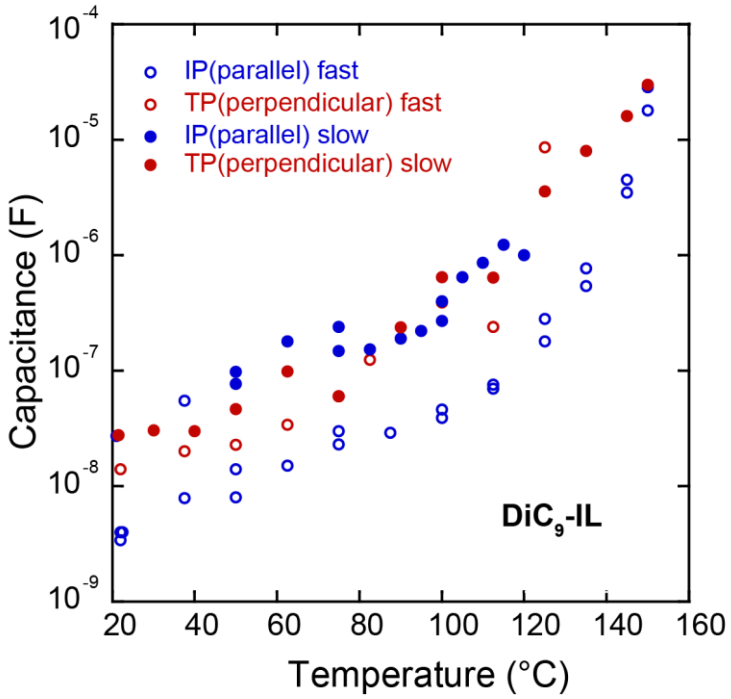

Figure S2. Capacitances of DiC_9-IL supramolecular complex extracted from the EIS measurements performed at two cooling scan rates (fast, 5 °C min^{-1}, and slow, 0.5 °C·min^{-1}) for the parallel and perpendicular geometries. The average error is of *ca.* 15 %.

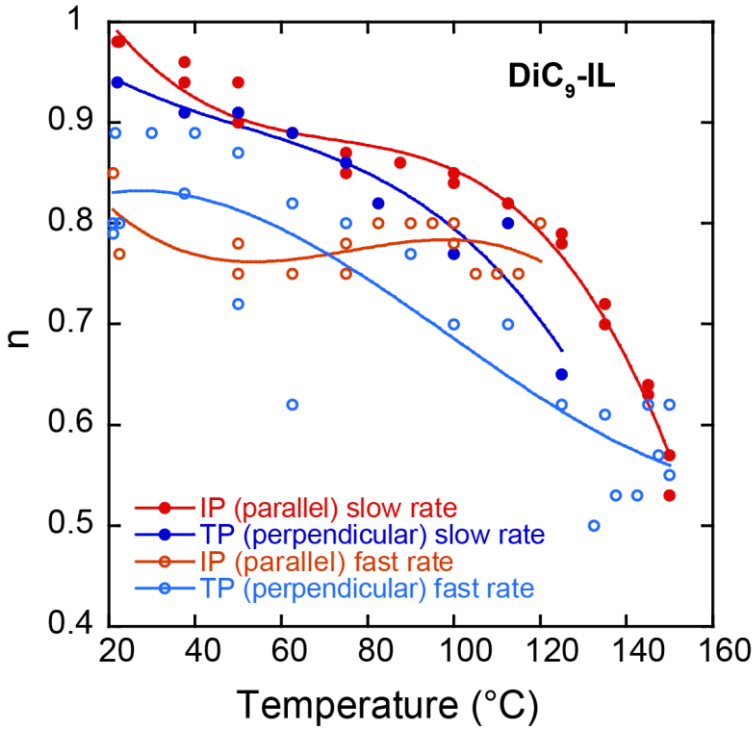

Figure S3. Temperature-dependent evolution of the *n* parameter of DiC_9-IL extracted from EIS experiments performed at two cooling scan rates (fast, 5 °C·min^{-1}, and slow, 0.5 °C·min^{-1}) for the parallel and perpendicular geometries. The average error is of *ca.* 0.1.

The variation of *n* with the temperature (See Figure S3) is consistent with a homogeneous bulk complex at slow cooling scan rate with *n* of *ca.* 0.95 at low temperature, in particular in the 20-40 °C temperature range. The *n* value remains constant from 20 up to 120 °C for EIS characterization in the parallel configuration while it decreases with the temperature for EIS characterization in the perpendicular configuration. For a low *n* value (*n* ~ 0.72, α = -65°) value, the interface is experiencing a transition toward an insulating regime. For the fast cooling scanning rate, the lack of organization and the related increasing disorder led to inhomogeneity. For the slow cooling scanning rate, *n* decreases with the temperature, EIS measurements in perpendicular configuration confirm the parallel long-range organization with a transport though a phase becoming less ionically conductive.

For C_X-IL supramolecular complexes (See Figures S4a-c), the behaviors of the electrolytes are characteristic of the bulk *vs.* the grain boundary (GB) contributions.

Between 22 and 40 °C, the addition in series of a Cole element for the bulk, and a finite length Warburg (short circuit terminus) for the GBs, describe an electrolyte with bulk and reflective boundary contributions. Three parameters define this Warburg element:
Ws-R are the diffusion impedance,
Ws-P is an exponential factor, the number 0.5 means the Warburg diffusion,
Ws-T means "diffusion interpretation" and has an equation: L^2/D, L and D being the diffusion layer thickness and the diffusion coefficient, respectively. Ws-T has a unit of s, considering L^2 as cm^2 and D as $cm^2 \cdot s^{-1}$, meaning the time for diffusion in the boundary.

Moreover, this model (R_1-ColeElement-ShortWarburg) fits very well the data. Between 42 and 70 °C, the GBs are more conductive (*e.g.* as in ceramic-type electrolytes) and two Cole elements have to be used. Between 70 and 150 °C, impedance diagrams are typical of isotropic electrolytes with no GB. The temperatures are indicative of transitions. All extracted parameters are consistent with the assumed variations of the C_X-IL electrolytes as a function of the temperature and the related phenomenological models fit well the different impedances diagrams.

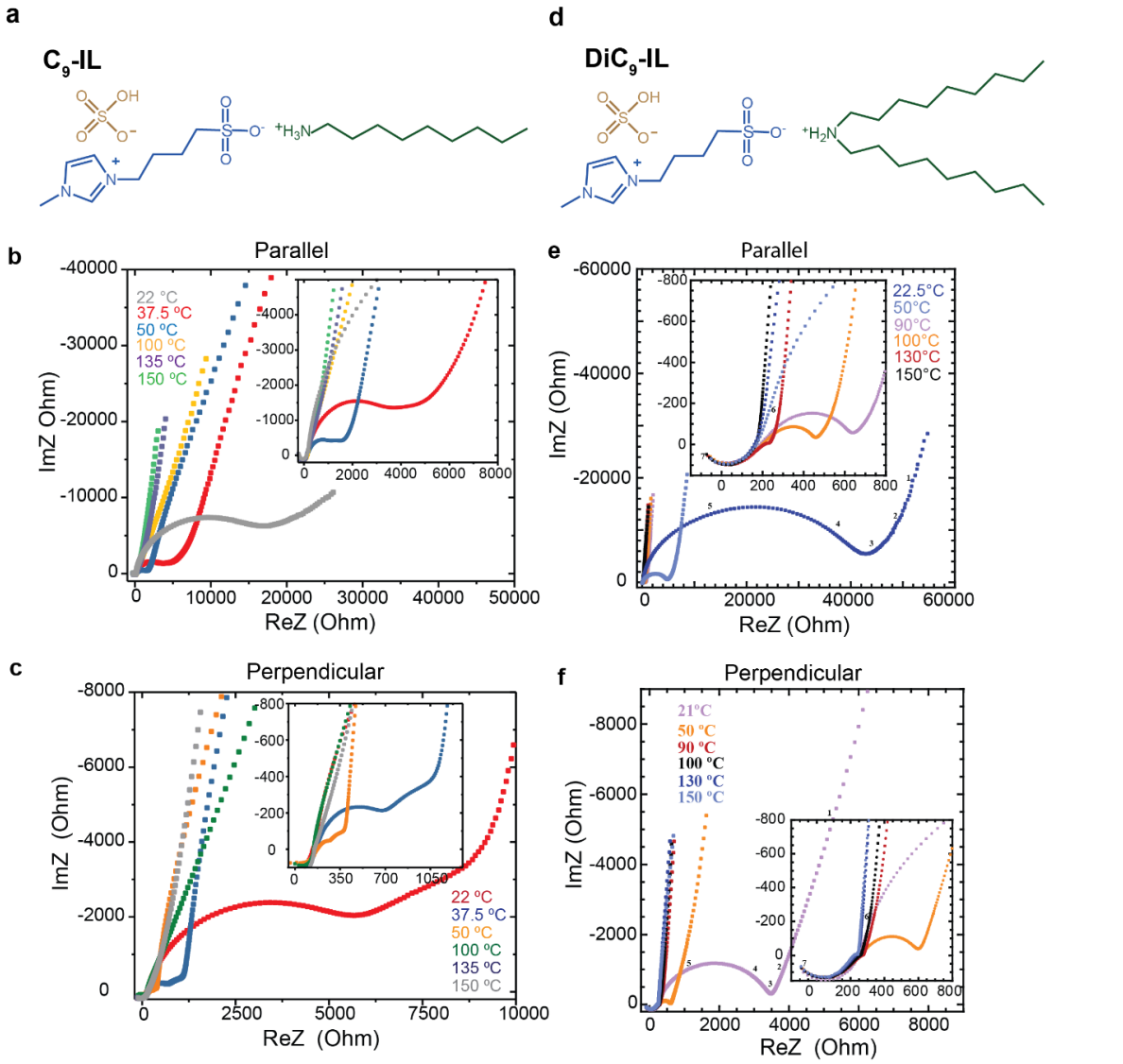

Figure S4. Representative Nyquist plots of C_9-IL and DiC_9-IL supramolecular complexes as a function of temperature. a) *n*-nonylamine 1-(4-sulfobutyl)-3-methylimidazolium hydrogen sulfate (C_9-IL). b) Temperature-dependent impedance spectra in the parallel configuration for a set of selected temperatures for C_9-IL. The inset shows the impedance behavior in the high frequency region of the Nyquist plots. c) Temperature-dependent impedance spectra in the perpendicular configuration for a set of selected temperatures for C_9-IL. The inset shows the impedance behavior in the high frequency region of the Nyquist plots. d) di-*n*-nonylamine 1-(4-sulfobutyl)-3-methylimidazolium hydrogen sulfate (DiC_9-IL). e) Temperature-dependent impedance spectra in the parallel configuration for a set of selected temperatures for DiC_9-IL. The inset shows the impedance behavior in the high frequency region of the Nyquist plots. f) Temperature-dependent impedance spectra in the parallel configuration for a set of selected temperatures for DiC_9-IL. The decades in frequency are mentioned. The inset shows the impedance behavior in the high frequency region of the Nyquist plots.

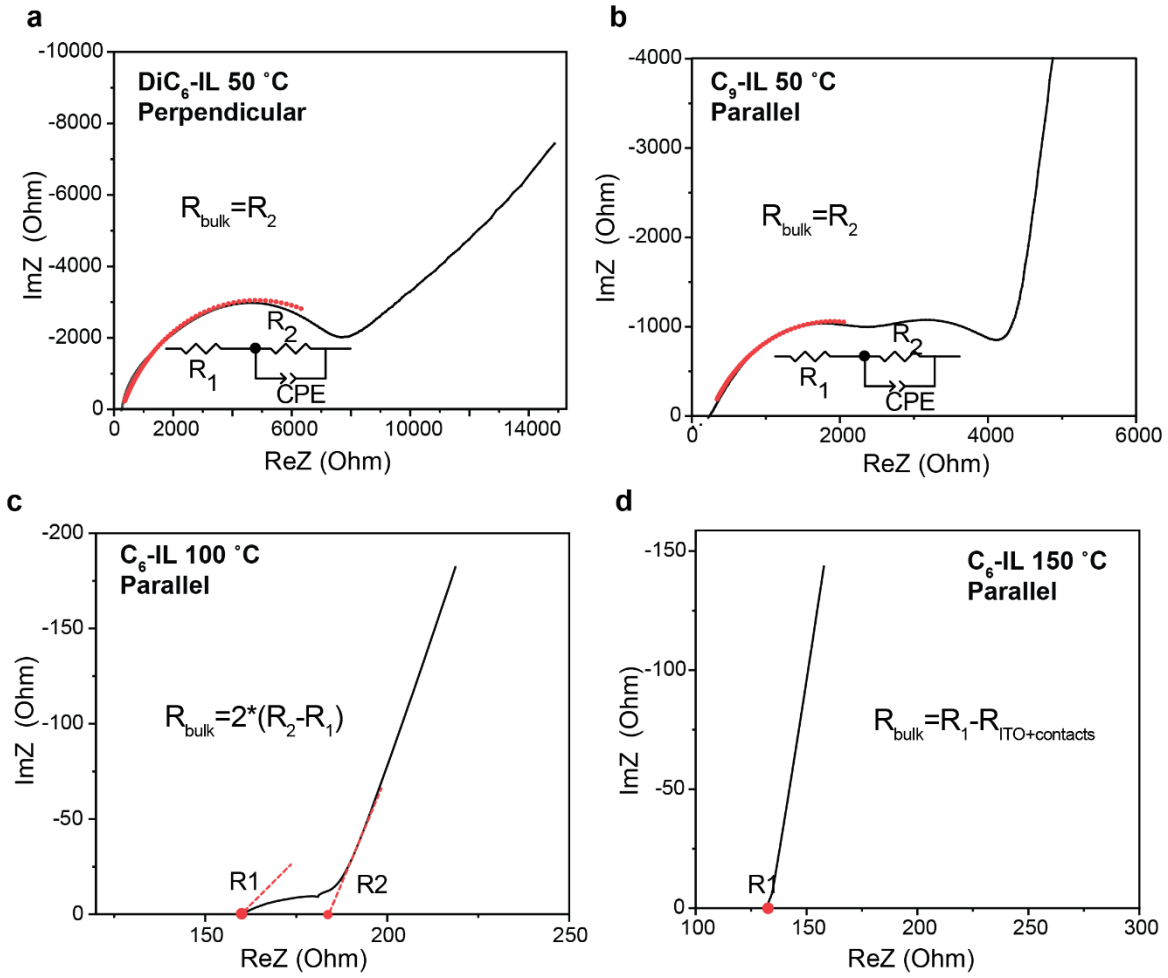

Figure S5. Method to analyze the Nyquist plots of impedance and the corresponding fitting procedure. a) Bulk resistance (R_{bulk}) extracted by fitting a semicircle to an electrical circuit model. R_1 represents the resistance due to the ITO electrodes, and connections and cables. R_2 represents bulk resistance of the sample and CPE represents the non-ideal capacitance of the sample. b) Bulk resistance (R_{bulk}) extracted by fitting the first semicircle with respect to the electrical model circuit. R_1 represents the resistance due to the ITO electrodes, connections and cables. R_2 represents bulk resistance of the sample. c) Bulk resistance (R_{bulk}) extracted by finding the high frequency Re*Z* intercept of the Nyquist plot (R_1) and the Re*Z* intercept of the extrapolated diffusive line (R_2). d) Bulk resistance (R_{bulk}) extracted by finding the high frequency Re*Z* intercept of the Nyquist plot (R_1) and then removing the resistance due to ITO electrodes, connections, and cables. The resistance due to ITO electrodes, connections, and cables were measured using ionic liquid 1-decyl-3-methylimidazolium bis[(trifluoromethyl)sulfonyl]imide (IoLiTec, Ref IL-0100-HP, CAS Number [433337-23-6], Purity > 98 %).

Diffusion coefficient

From the general diffusion equations of a particle, the following relationship gives the order of magnitude for a diffusion coefficient:

$$<l^2> = f_i.D\cdot\tau$$

where l is the mean distance from the starting point that an ion will have diffused during time τ, f_i is a numerical constant which depends on dimensionality (f_i = 2, 4, or 6 for 1D, 2D, or 3D-diffusion, respectively), D is the diffusion coefficient (in $cm^2\cdot s^{-1}$), and τ (in s) the time of diffusion obtained by EIS.

In the present case, $D = <l^2>/4\tau$ since the supramolecular complexes have shown long-range 2D organization, as revealed by XRD. Considering that an ion can explore, in each direction, in the plane defined by the b and c axes, $l_{min} = 2\cdot l_c$, l_c being the correlation length of the periodicity along the c axis, it turns out that $D = l_c^2/\tau$.

The statistical approach is consistent in our case at the micron scale. The relation between the diffusion coefficient D and the distance l that an ion can go through when diffusing in a time τ is $D = l^2/2\tau$. It correlates the microscopic details of ion diffusion and the macroscopic quantities associated with the diffusion, such as the long-range ordering taking place within the supramolecular complexes sandwiched in between electrodes. The equation is derived by assuming that ions undergo a random walk. Note importantly that the order of magnitude for the diffusion coefficient remains the same as the one obtained with the classical approach.

Supporting Note 2: On the subtlety of the highest temperature phases in the surfactant-induced ionic liquid crystals

The supramolecular nature of these surfactant-induced ionic liquid crystals involves subtleties in their thermal behavior when compared to classic ionic liquid crystals. At the highest temperatures, covalently bonded ionically conductive liquid crystals typically possess an isotropic phase[S6]. Therein, even if the ion conductivity is anisotropic at lower temperature due to the self-assembled conducting and aligned channels, the conductivity is isotropic at temperature higher than the clearing point.

Strikingly, the ion transport behavior of the present surfactant self-assembled ionic liquid crystals is different. We noticed fully reversible behavior in heating and cooling scans, even upon prolonged annealing (up to a few hours), when the temperature was kept lower than 150 °C. Up to such temperatures, SAXS characterizations indicated lamellar self-assembly (Figures 2d-f in the main text and Supporting Figure S13). This agrees very well

with the ion conductivity measurements displayed in Figure 3c in the main text which shows strong anisotropy up to *ca.* 150 °C.

Can one achieve isotropic phase in C_xIL and DiC_xIL supramolecular complexes?

Even if the ionic bond between the positively charged protonated *n*-alkylamines (or di-*n*-alkylamines) and negatively charged deprotonated sulfonic acid groups can be considered to be strong in these surfactant self-assembled ionic liquid crystals, at elevated temperatures the bonding becomes strained by thermal energy. Upon sufficient heating it is expected that the bonding will be weakened, and eventually that a fraction of uncomplexed 1-(4-sulfobutyl)-3-methylimidazolium hydrogen sulfate with free sulfonic acid end groups will dissociate. Combining with high temperature, the underlying strong acidity is expected to lead to detrimental side-reactions onto the ITO electrodes of LC cells. To directly study the effect of free sulfonic acid end group onto the ITO electrodes of the LC cells, the impact of chemical side-reactions of uncomplexed 1-(4-sulfobutyl)-3-methylimidazolium hydrogen sulfate are directly evidenced in Figure S26.

In the numerous repeated experiments performed in this research, we emphasize here that no such detrimental effects were observed upon prolonged (up to a few hours) annealing supramolecular complexes below *ca.* 150 °C.

To conclude, phase separation of the supramolecular complexes leading to free surfactants and ionic liquids which can trigger side-reactions with ITO electrodes that will take place upon excessive heating (higher than the clearing point) or prolonged annealing at temperature of *ca.* 155 °C. Thus, the regime for isotropic ion transport cannot be measured for this series of supramolecular ionic liquid crystals to preserve their chemical integrity.

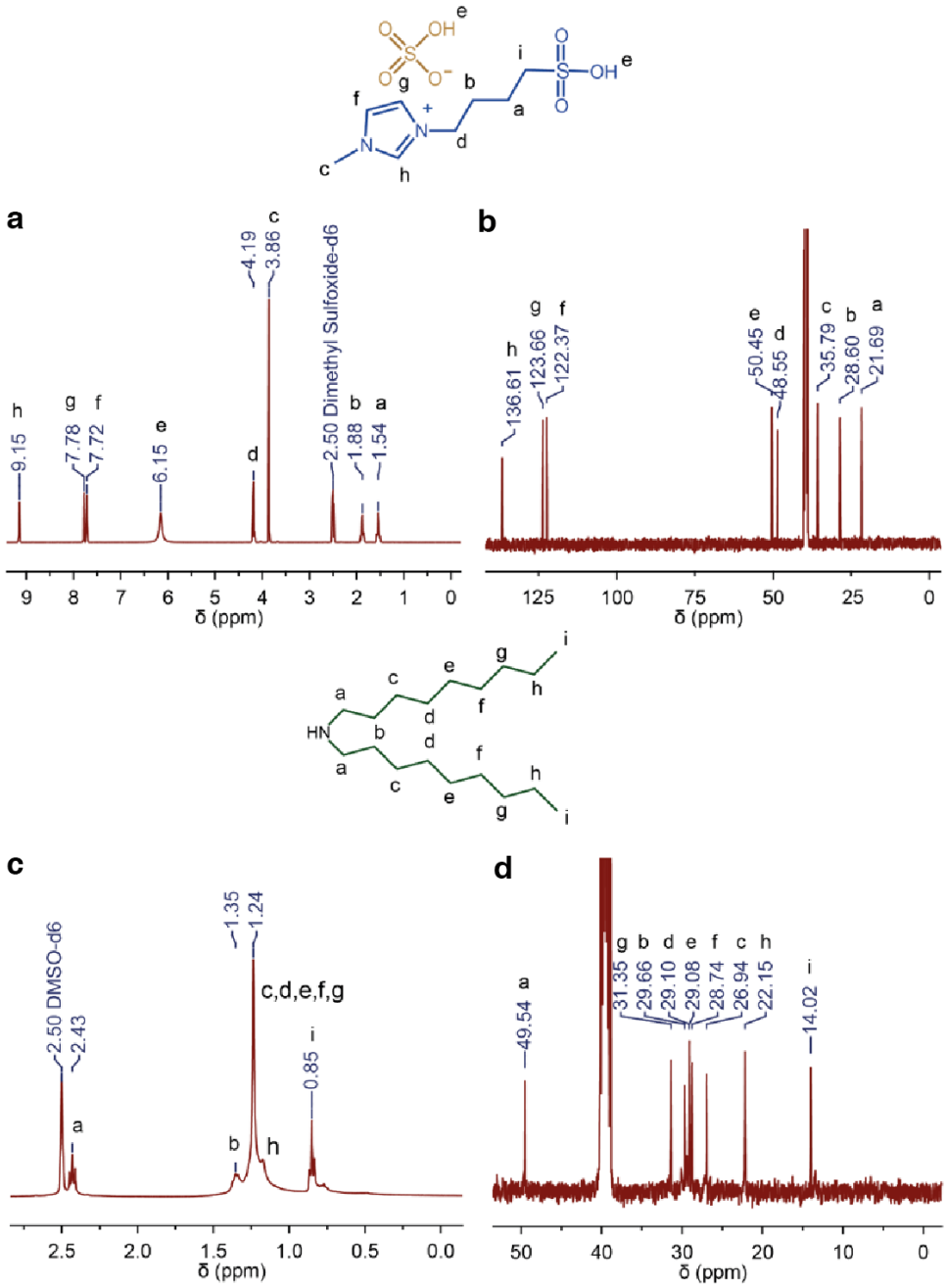

Figure S6. NMR spectra of 1-(4-sulfobutyl)-3-methylimidazolium hydrogen sulfate (IL) and di-*n*-nonylamine (DiC_9). a) ^{1}H NMR spectrum of IL. b) ^{13}C NMR spectrum of IL. c) ^{1}H NMR spectrum of DiC_9. d) ^{13}C NMR spectrum of DiC_9.

a) IL ^{1}H NMR (400 MHz, DMSO-d_6) δ (ppm) 9.15, 7.78, 7.72, 6.15, 4.19, 3.86, 2.50, 1.88, 1.54.

b) IL ^{13}C NMR (101 MHz, DMSO-d_6) δ (ppm) 136.61, 123.66, 122.37, 50.45, 48.55, 39.52, 35.79, 28.60, 21.69.

c) DiC_9 ^{1}H NMR (400 MHz, DMSO-d_6) δ (ppm) 3.36, 2.50, 2.43, 1.35, 1.24, 0.85.

d) DiC_9 ^{13}C NMR (101 MHz, DMSO-d_6) δ (ppm) 49.54, 39.52, 31.35, 29.66, 29.10, 29.08, 28.74, 26.94, 22.15, 14.02.

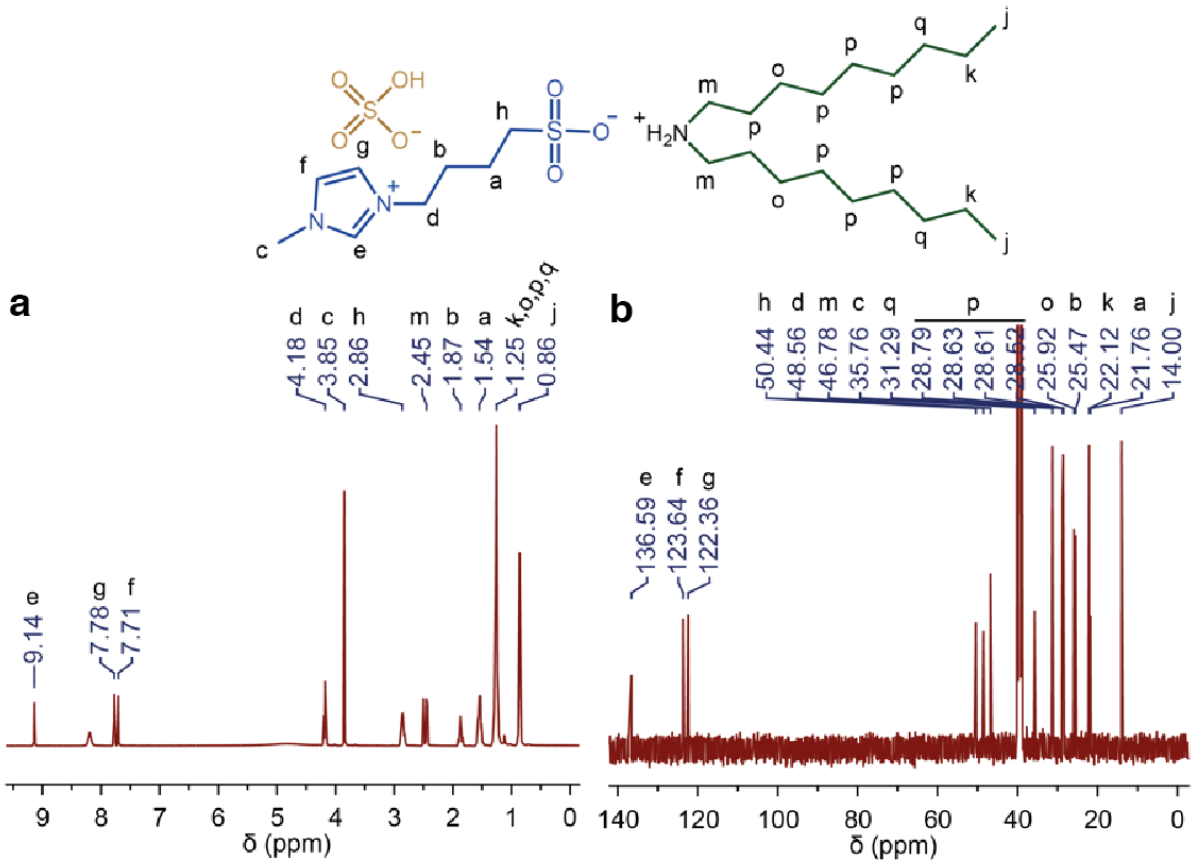

Figure S7. NMR-spectra of the di-*n*-nonyl 1-(4-sulfobutyl)-3-methylimidazolium hydrogen sulfate (DiC_9-IL) supramolecular complex a) ^{1}H NMR spectrum of DiC_9-IL. b) ^{13}C NMR spectrum of DiC_9-IL.

a) DiC_9-IL ^{1}H NMR (400 MHz, DMSO-d_6) δ (ppm) 9.14, 7.78, 7.71, 4.18, 3.85, 2.86, 2.50, 2.45, 1.87, 1.54, 1.25, 0.86.

b) DiC_9-IL ^{13}C NMR (101 MHz, DMSO-d_6) δ (ppm) 136.59, 123.64, 122.36, 50.44, 48.56, 46.78, 39.52, 35.76, 31.29, 28.79, 28.63, 28.61, 28.52, 25.92, 25.47, 22.12, 21.76, 14.00.

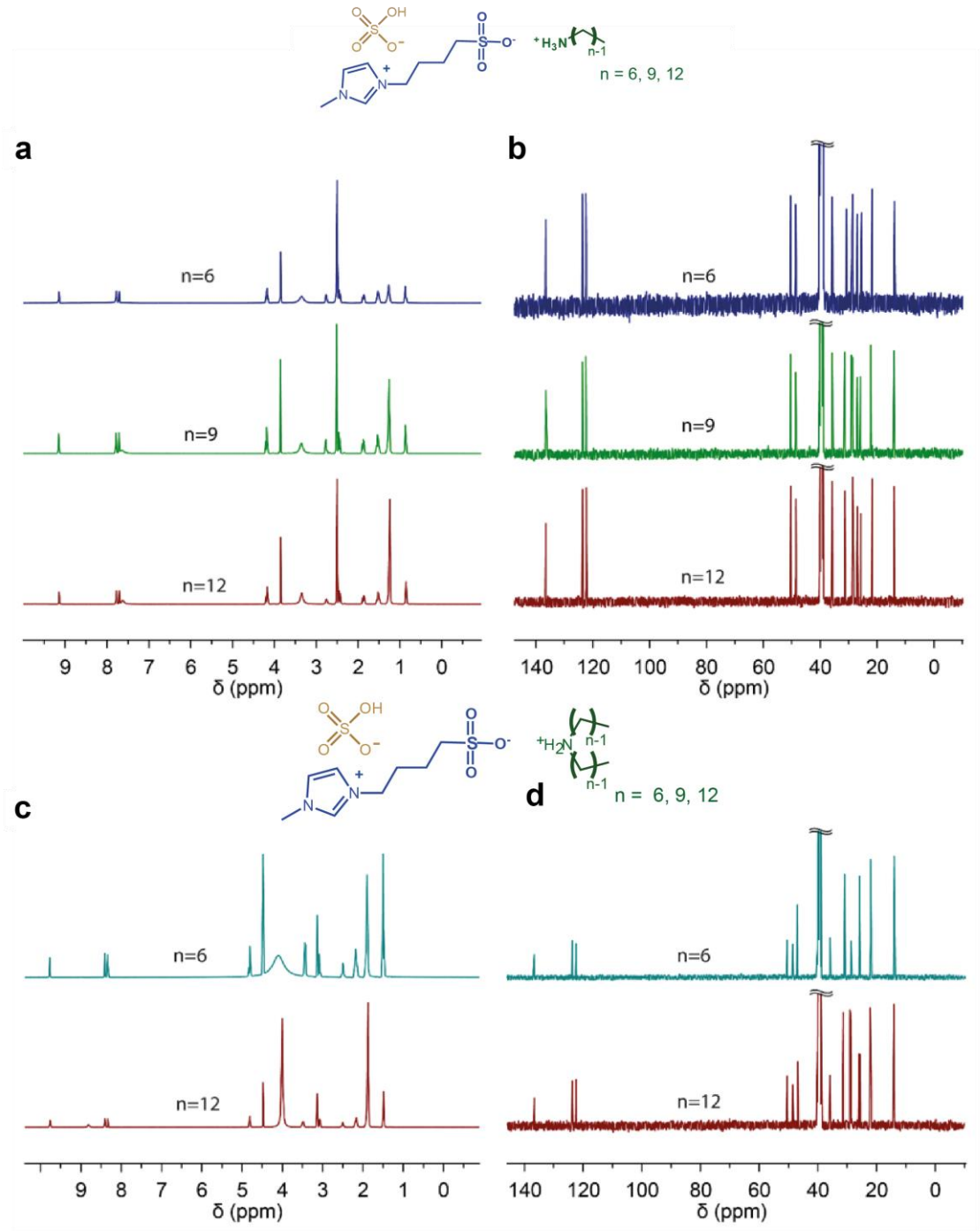

Figure S8. NMR spectra of surfactant-induced self-assembled supramolecular ionic liquid crystals. a) ^{1}H NMR of C_6-IL (n=6), C_9-IL (n=9), and C_{12}-IL (n=12). b) ^{13}C NMR of C_6-IL (n=6), C_9-IL (n=9), and C_{12}-IL (n=12). c) ^{1}H NMR of DiC_6-IL (n=6) and DiC_{12}-IL (n=12). d) ^{13}C NMR of DiC_6-IL (n=6) and DiC_{12}-IL (n=12).

a) C_6-IL ^{1}H NMR (400 MHz, DMSO-d_6) δ (ppm) 9.14, 7.78, 7.71, 4.18, 3.85, 2.76, 2.50, 2.45, 1.87, 1.52, 1.26, 0.87.

a) C_9-IL ^{1}H NMR (400 MHz, DMSO-d_6) δ (ppm) 9.14, 7.78, 7.71, 7.64, 4.18, 3.85, 3.35, 2.76, 2.50, 2.45, 1.87, 1.53, 1.25, 0.86.

a) C_{12}-IL ^{1}H NMR (400 MHz, DMSO-d_6) δ (ppm) 9.14, 7.78, 7.71, 7.62, 4.18, 3.85, 3.35, 2.76, 2.50, 2.45, 1.87, 1.52, 1.24, 0.85.

b) C_6-IL ^{13}C NMR (101 MHz, DMSO-d_6) δ (ppm) 136.59, 123.64, 122.36, 50.44, 48.57, 40.28, 39.52, 35.77, 30.75, 28.63, 27.00, 25.49, 21.94, 21.77, 13.88.

b) C_9-IL ^{13}C NMR (101 MHz, DMSO-d_6) δ (ppm) 136.53, 123.58, 122.30, 50.38, 48.50, 35.70, 31.23, 28.76, 28.57, 28.55, 28.49, 26.94, 25.74, 22.06, 21.71, 13.94.

b) C_{12}-IL ^{13}C NMR (101 MHz, DMSO-d_6) δ (ppm) 136.59, 123.64, 122.36, 50.44, 48.57, 39.52, 35.77, 31.33, 29.08, 29.05, 28.96, 28.87, 28.75, 28.64, 28.55, 27.00, 25.80, 22.13, 21.77, 14.01.

c) DiC_6-IL ^{1}H NMR (400 MHz, DMSO-d_6) δ (ppm) 9.14, 7.77, 7.70, 4.18, 3.85, 3.47, 2.81, 2.50, 2.45, 1.87, 1.54, 1.26, 0.87.

c) DiC_{12}-IL ^{1}H NMR (400 MHz, DMSO-d_6) δ (ppm) 9.12, 8.18, 7.77, 7.70, 4.18, 3.85, 2.85, 2.50, 2.45, 1.87, 1.54, 1.24, 0.85.

d) DiC_6-IL ^{13}C NMR (101 MHz, DMSO-d_6) δ (ppm) 136.61, 123.66, 122.38, 50.45, 48.59, 46.99, 39.52, 35.79, 30.83, 28.65, 25.80, 25.76, 21.98, 21.77, 13.92.

d) DiC_{12}-IL ^{13}C NMR (101 MHz, DMSO-d_6) δ (ppm) 136.59, 123.66, 122.38, 50.44, 48.60, 46.79, 39.52, 35.79, 31.35, 29.09, 29.07, 28.97, 28.84, 28.77, 28.64, 28.53, 25.93, 25.50, 22.15, 21.77, 14.02.

Below are listed the chemical shifts (^{1}H and ^{13}C NMR) for the C_6 and C_{12} *n*-alkylamine and DiC_6 and DiC_{12} di-*n*-alkylamine surfactants (spectra not shown):

C_6 ^{1}H NMR (400 MHz, $CDCl_3$) δ (ppm) 7.26, 2.58, 1.47, 1.27, 1.25, 0.88.

C_6 ^{13}C NMR (101 MHz, DMSO-d_6) δ (ppm) 41.79, 39.52, 33.52, 31.32, 26.17, 22.19, 13.97.

C_9 ^{1}H NMR (400 MHz, DMSO-d_6) δ (ppm) 2.50, 2.47, 1.29, 1.24, 0.85.

C_9 ^{13}C NMR (101 MHz, DMSO-d_6) δ (ppm) 41.73, 33.52, 31.29, 29.06, 29.04, 28.69, 26.45, 22.08, 13.92.

C_{12} ^{1}H NMR (400 MHz, DMSO-d_6) δ (ppm) 3.33, 2.50, 2.47, 1.24, 0.85.

C_{12} ^{13}C NMR (101 MHz, DMSO-d_6) δ (ppm) 41.79, 39.52, 33.55, 31.35, 29.16, 29.12, 29.09, 29.07, 28.77, 26.52, 22.15, 14.00.

DiC_6 ^{1}H NMR (400 MHz, DMSO-d_6) δ (ppm) 3.35, 2.50, 2.44, 1.36, 1.24, 0.85.

DiC_6 ^{13}C NMR (101 MHz, DMSO-d_6) δ (ppm) 49.60, 39.52, 31.37, 29.67, 26.65, 22.18, 13.99.

DiC_{12} ^{1}H NMR (400 MHz, $CDCl_3$) δ (ppm) 7.26, 2.58, 1.47, 1.27, 1.25, 0.88.

DiC_{12} ^{13}C NMR (101 MHz, $CDCl_3$) δ (ppm) 77.16, 50.32, 32.07, 30.34, 29.82, 29.79, 29.77, 29.75, 29.50, 27.58, 22.84, 14.28.

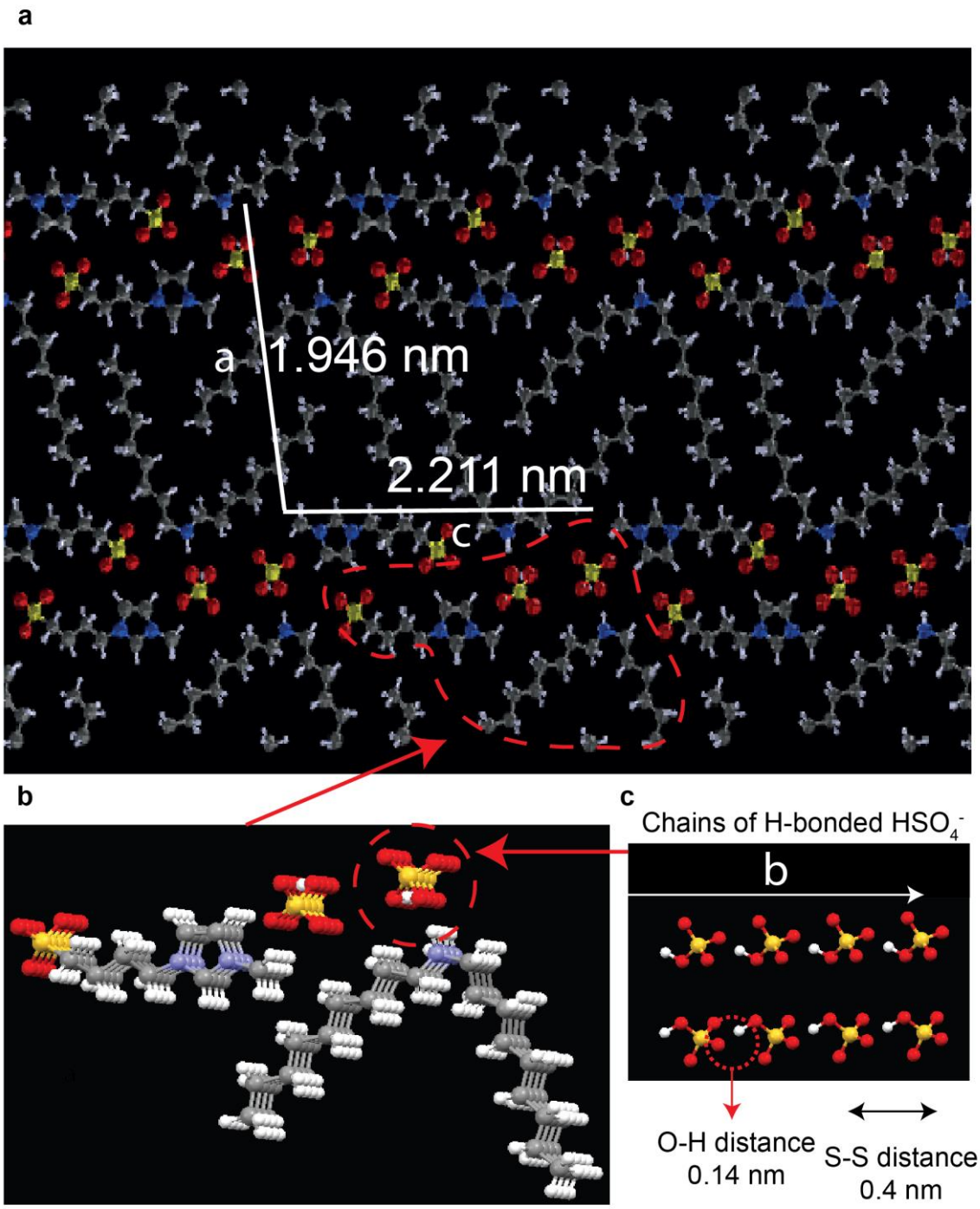

Figure S9. DFT optimized structure of the DiC_9-IL supramolecular complex at 25 °C. a) Enlarged image of DFT optimized structure of DiC_9-IL at 25 °C (*vs.* Figure 3b in the main text), forming a monoclinic unit cell. b) Slightly tilted packing to visualize the arrangement of molecules onto the *b* axis of the unit cell. c) Chains of H-bonded HSO_4^- counter ions in the direction of the *b* axis of unit cell.

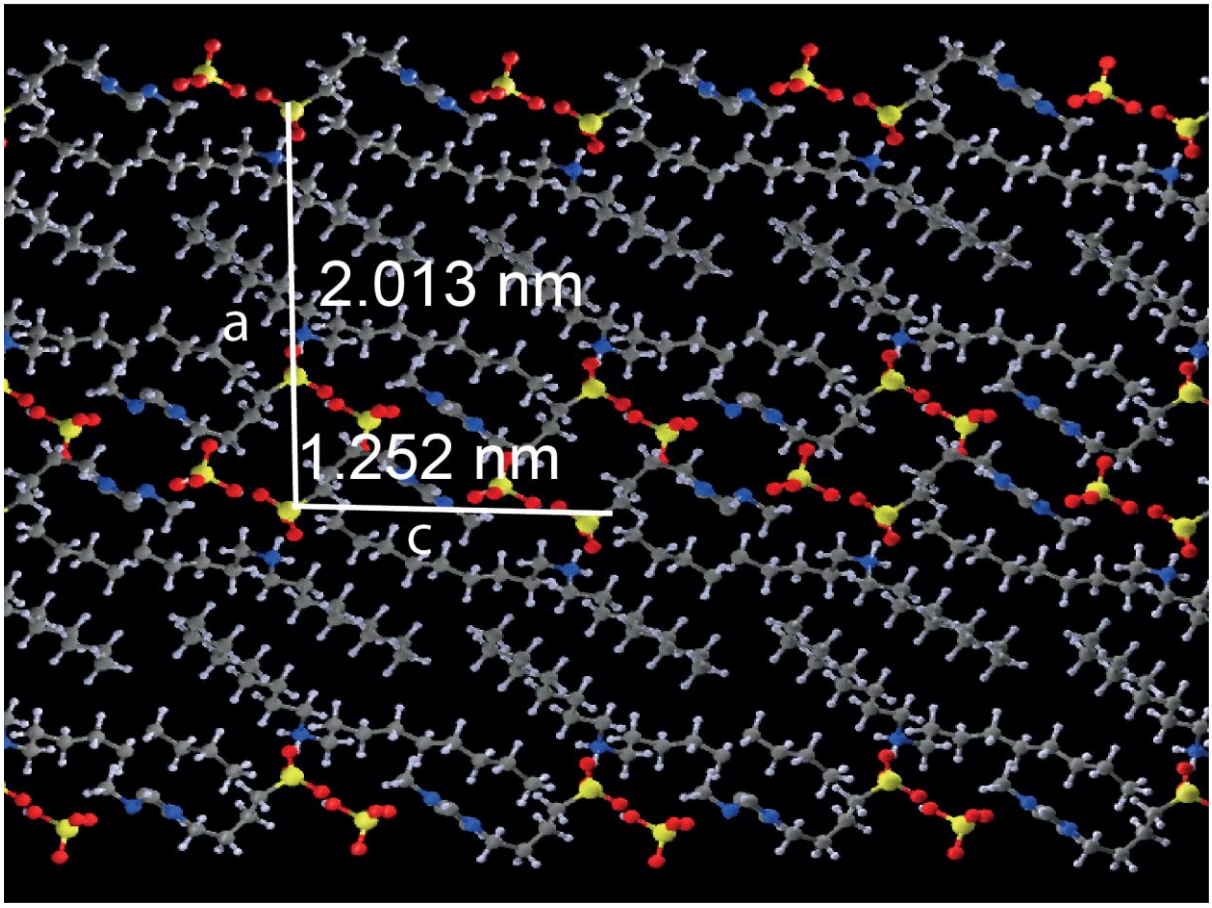

Figure S10. DFT optimized structure of the DiC_9-IL supramolecular complex at 150 °C, enlarged version of Figure 2e of the main text.

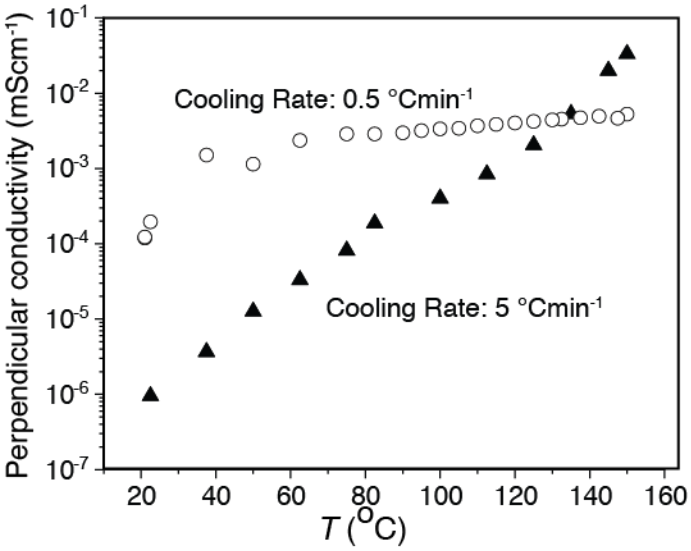

Figure S11. Effect of cooling rate on the perpendicular ion conductivity of the DiC_9-IL supramolecular complex. A fast cooling rate of 5 °C·min^{-1} gives a thermally activated ion transport behavior while a slow cooling rate of 0.5 °C·min^{-1} gives almost no temperature activation. This could be a result of fewer "leakage channels" due to well-formed smectic

layers when slowly cooled. To the contrary, with a fast cooling rate poorly formed smectic layers with leakage channels would form, leading to thermally activated ion transport.

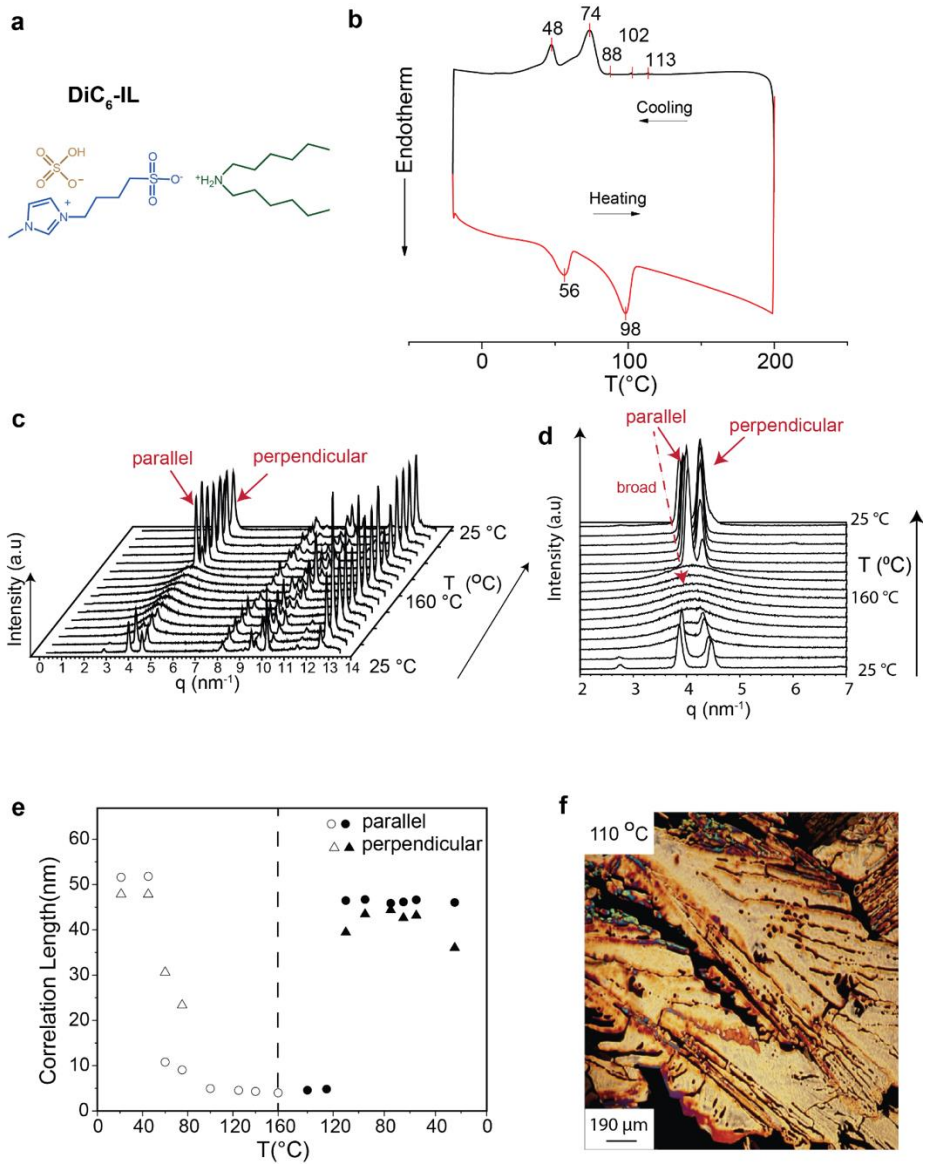

Figure S12. DSC, XRD, and POM characterizations of di-*n*-hexylamine 1-(4-sulfobutyl)-3-methylimidazolium hydrogen sulfate (DiC_6-IL). a) Chemical formula of the DiC_6-IL supramolecular complex. b) DSC of DiC_6-IL. c) XRD as a function of temperature. Based on the detailed analysis in DiC9-IL, we hypothesize that also DiC_6-IL shows qualitatively similar structure. Taken this hypothesis, we suggest to assign the low-*q* reflections as the *c* and *a* directions of the unit cell, representing directions parallel to the ionic layers (denoted *parallel*) and perpendicular to the ionic layers (denoted *perpendicular*), respectively. d) Development of the low angle peaks as a function of temperature. At high temperatures the peaks merge into a single broad peak. e) Correlation length parallel and perpendicular to the ionic layers as a function of temperature, extracted from the low angle peaks in d) At high temperatures correlation length parallel to the ionic layers reduces dramatically. f) POM microphotograph

captured by artificially generating defects to give a local birefringent and colorful homogeneously aligned mosaic texture while DiC_6-IL spontaneously form homeotropically alignment black area as its natural POM texture.

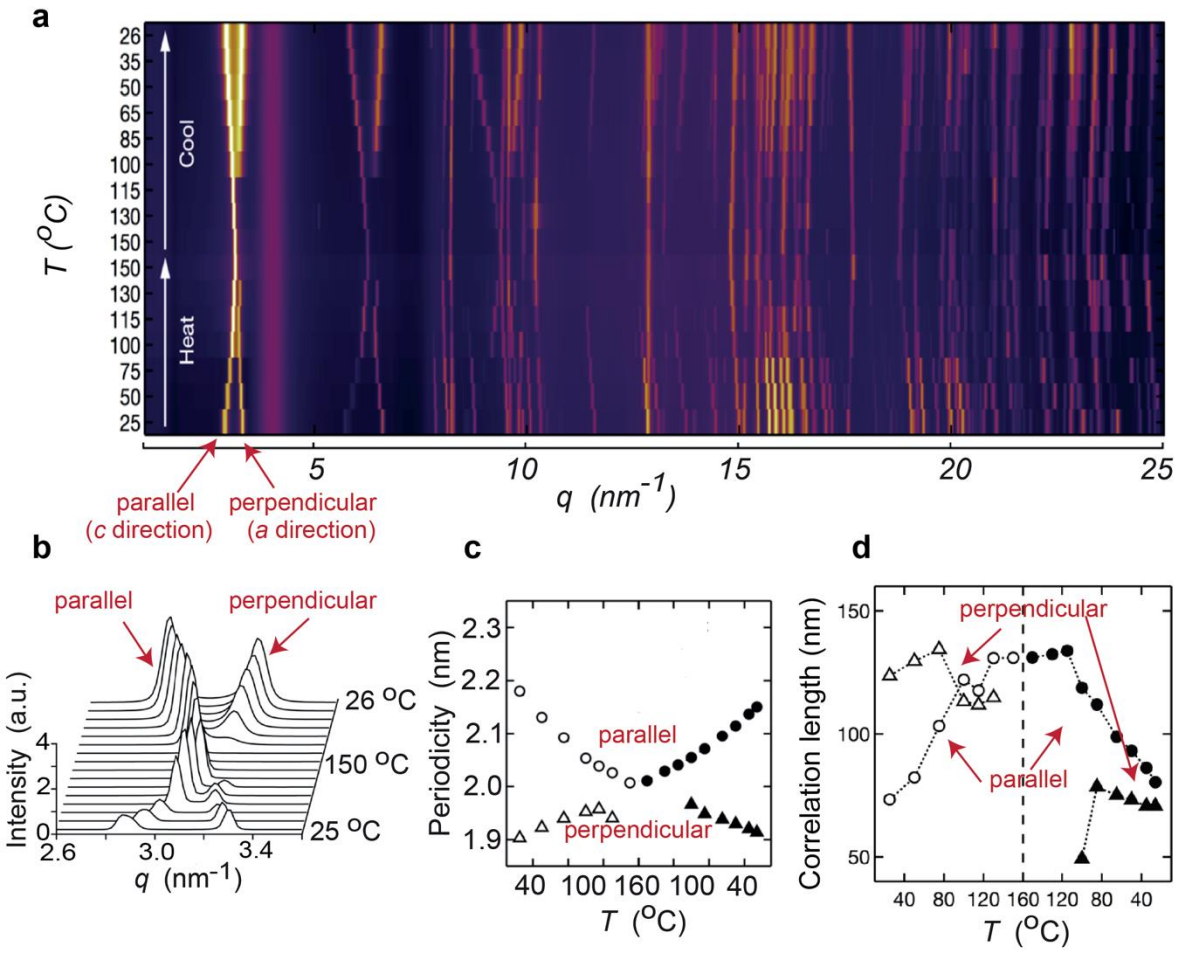

Figure S13. Synchrotron SAXS/WAXS 2D and 1D patterns of the DiC_9-IL supramolecular complex. a) SAXS/WAXS 2D scattering patterns upon consecutive heating and cooling scans. The intense *q* reflections are assigned to *c* and *a* directions of the monoclinic unit cell of the DFT optimized room temperature structure. The *c* and *a* directions of the unit cell represent directions parallel to the ionic layers (denoted *parallel*) and perpendicular to the ionic layers (denoted *perpendicular*) respectively. b) Development of *parallel* and *perpendicular* reflections as a function of temperature. At high temperature these reflections merge into one single sharp reflection. c) Development of corresponding periodicities. d) Correlation lengths parallel and perpendicular to the ionic layers as a function of temperature, extracted from *parallel* and *perpendicular* reflections in b) Correlation lengths parallel to the ionic layers constantly increase with temperature, indicating increasing long-range order with temperature. This also corresponds with decreasing mesoscopic characteristic times and promoted-ion transport at high temperatures (see Figure 3 of the main text).

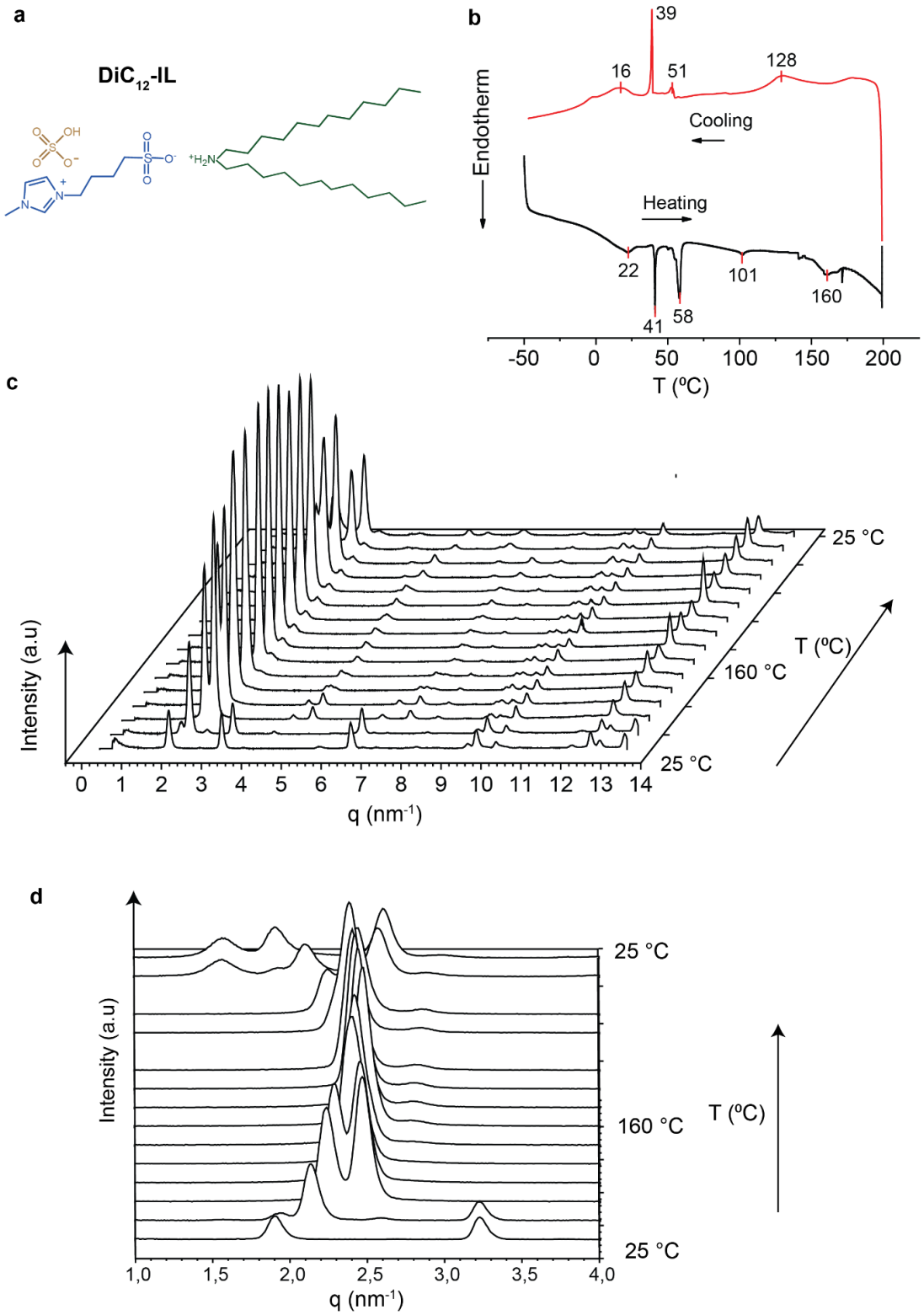

Figure S14. DSC and XRD characterizations of di-*n*-dodecylamine 1-(4-sulfobutyl)-3-methylimidazolium hydrogen sulfate (DiC_{12}-IL). a) Chemical formula of the DiC_{12}-IL supramolecular complex. b) DSC of DiC_{12}-IL. c) XRD as a function of temperature. d) Development of higher order reflections as a function of temperature.

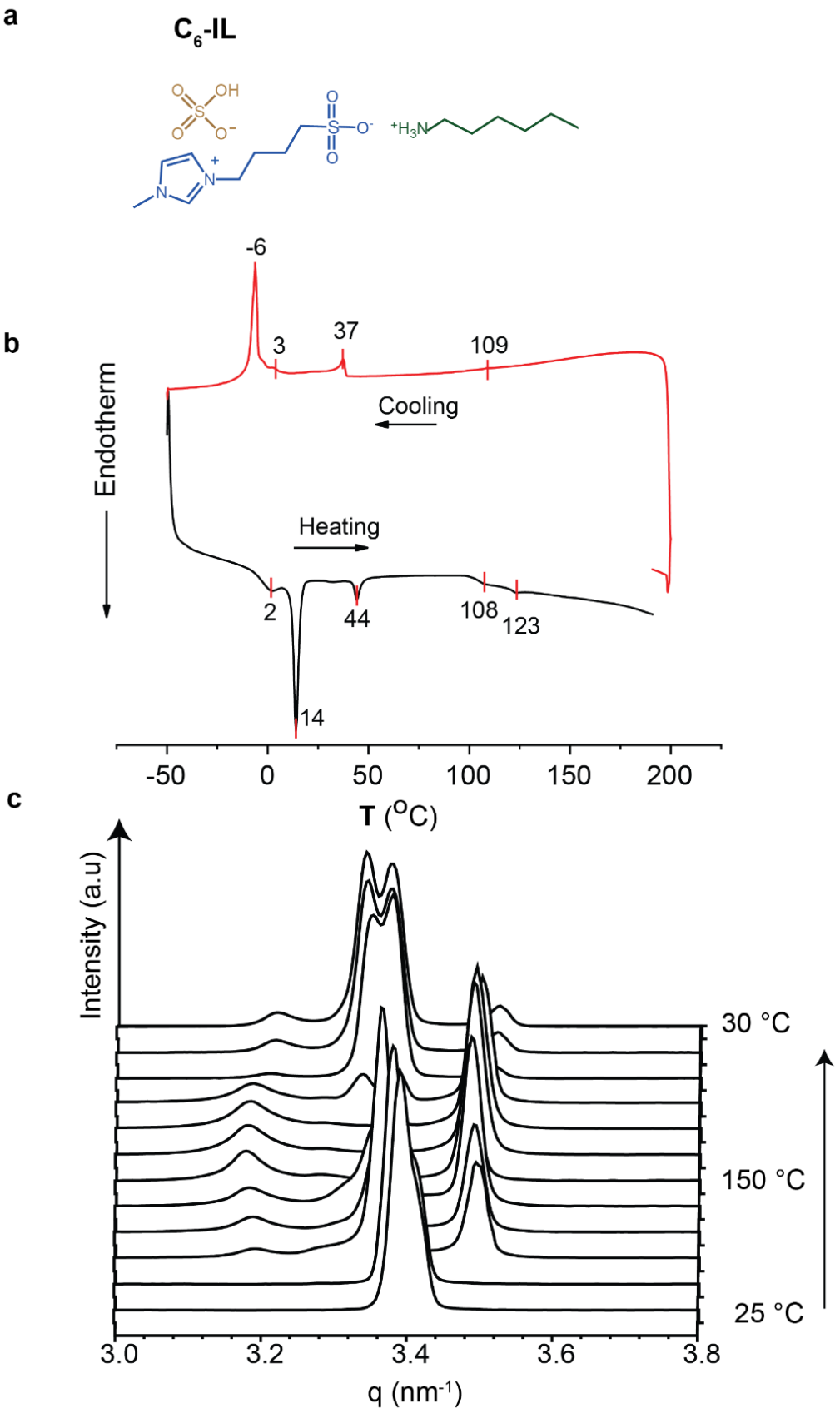

Figure S15. DSC and XRD characterizations of *n*-hexylamine 1-(4-sulfobutyl)-3-methylimidazolium hydrogen sulfate (C_6-IL). a) Chemical formula of the C_6-IL

supramolecular complex. b) DSC of C_6-IL. c) Development of the low *q* value reflections as a function of temperature.

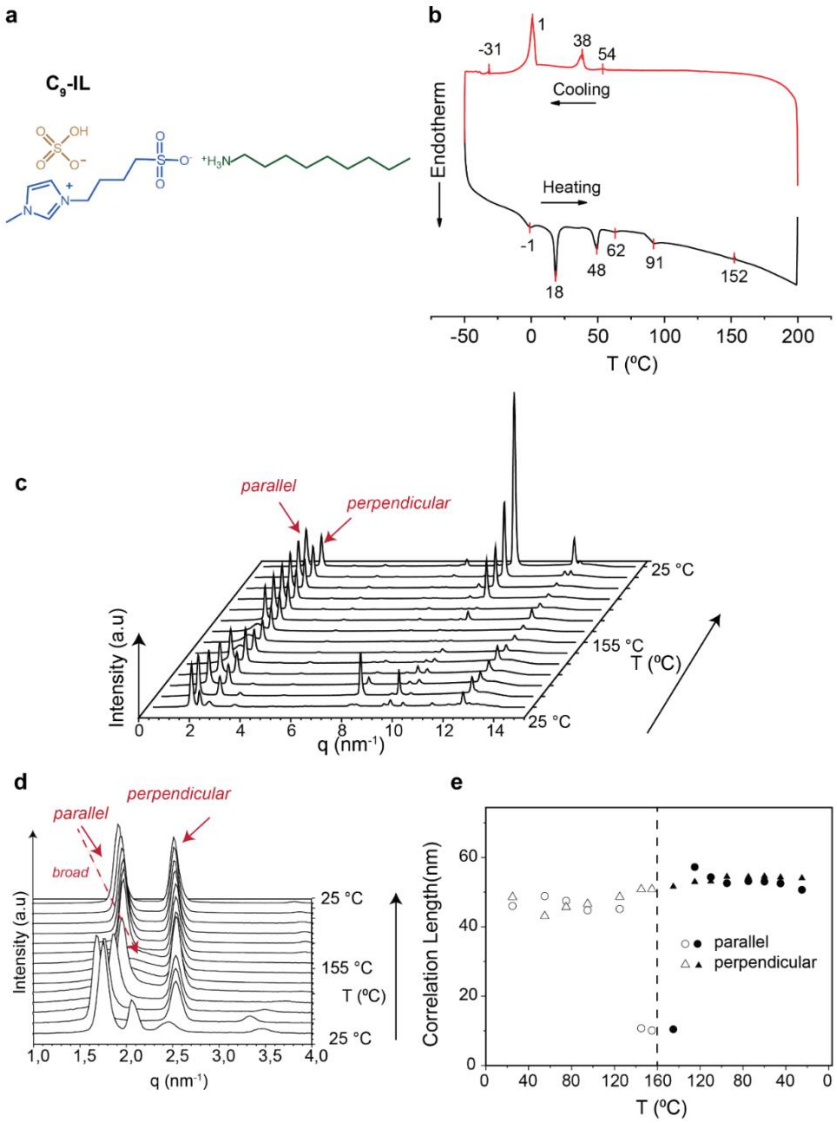

Figure S16. DSC and XRD characterizations of *n*-nonylamine 1-(4-sulfobutyl)-3-methylimidazolium hydrogen sulfate (C_9-IL). a) Chemical formula of the C_9-IL supramolecular complex. b) DSC of C_9-IL. c) XRD as a function of temperature, with the low *q* reflections. We tentatively hypothesize that they can be assigned to the *a* and *c* directions of the monoclinic unit cell of the DFT optimized room temperature structure, qualitatively similar as in DiC_9-IL. Taken this assumption, the *c* and *a* directions of the unit cell represent directions parallel to the ionic layers (denoted *parallel*) and perpendicular to the ionic layers (denoted *perpendicular*) respectively. d) Development of *parallel* and *perpendicular* reflections as a function of temperature. The *parallel* reflection develops into a single broad reflection at high temperature. e) Correlation lengths parallel and perpendicular to the ionic

layers as a function of temperature, extracted from *parallel* and *perpendicular* reflections in d) At high temperatures, the correlation lengths parallel to the ionic layers reduce dramatically due to the broadening of *parallel* reflection.

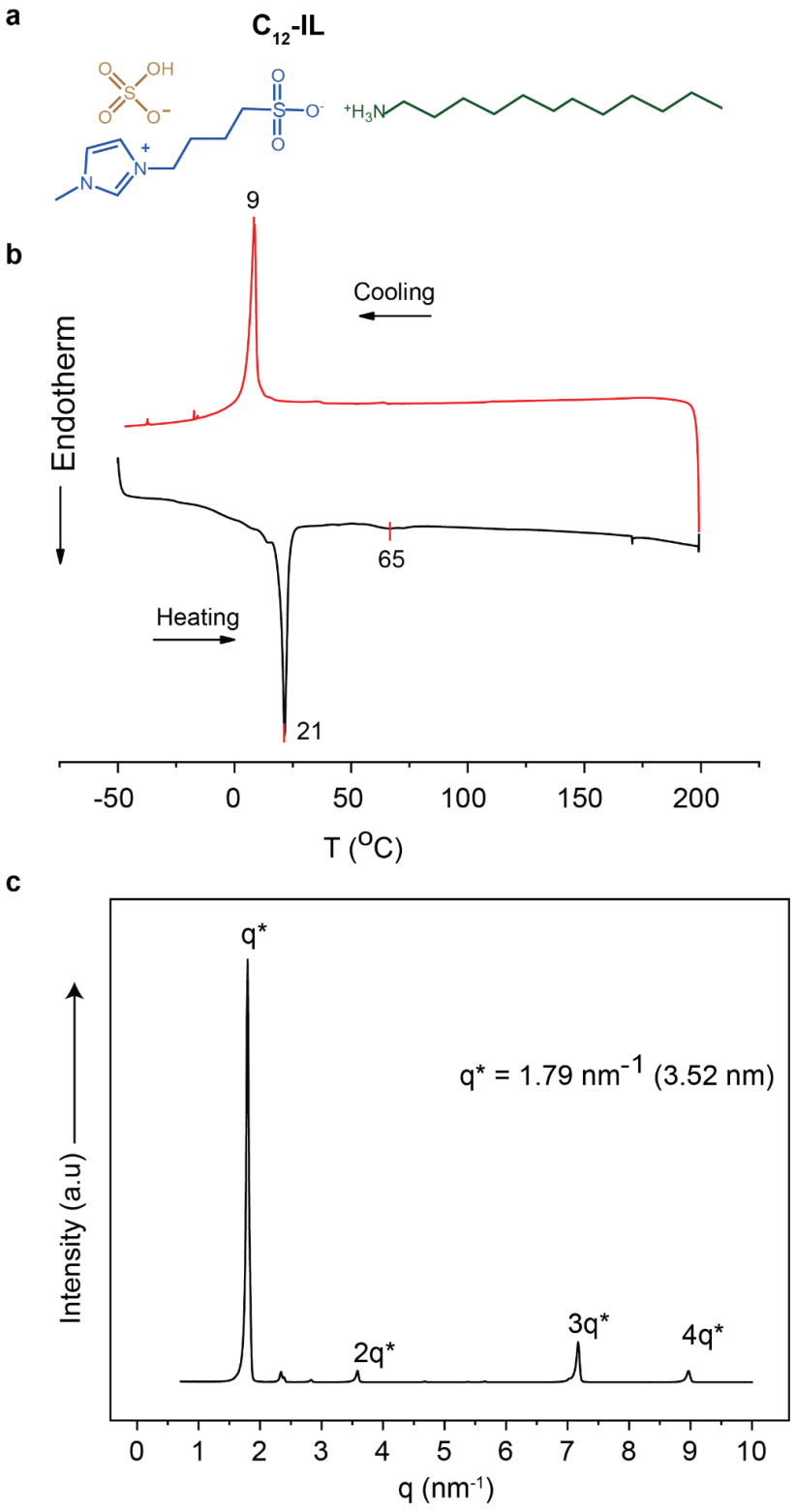

Figure S17. DSC and XRD characterizations of *n*-dodecylamine 1-(4-sulfobutyl)-3-methylimidazolium hydrogen sulfate (C_{12}-IL). a) Chemical formula of the C_{12}-IL

supramolecular complex. b) DSC of C_{12}-IL. c) Room temperature XRD of C_{12}-IL, showing lamellar order.

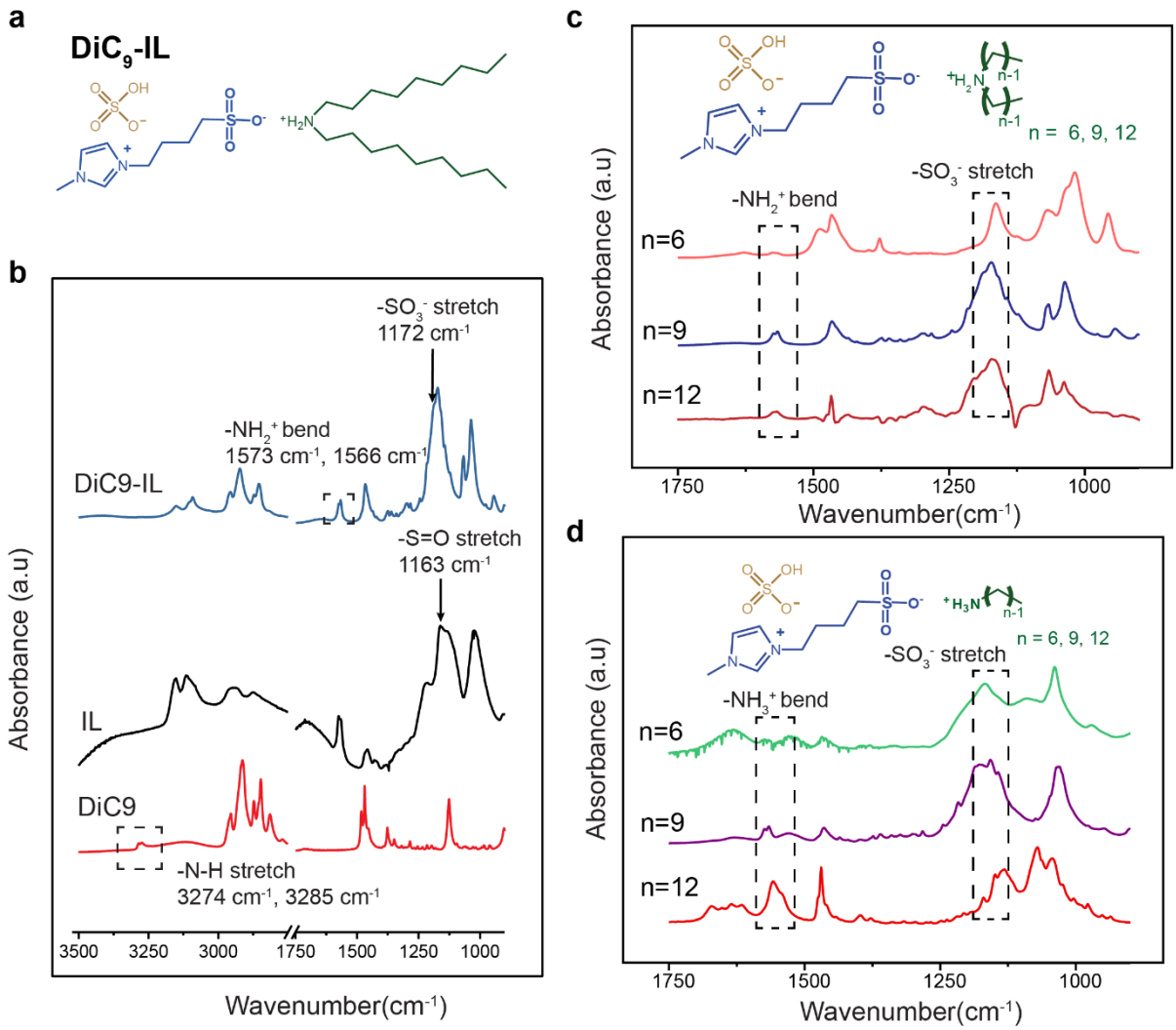

Figure S18. FTIR spectra of surfactant-induced self-assembled supramolecular ionic liquid crystals. a) Di-*n*-nonylamine 1-(4-sulfobutyl)-3-methylimidazolium hydrogen sulfate (DiC_9-IL). b) FTIR spectra of DiC_9-IL and its sub-components: di-*n*-nonylamine (DiC_9) and 1-(4-sulfobutyl)-3-methylimidazolium hydrogen sulfate (IL) with their corresponding characteristic absorptions. c) FTIR spectra of supramolecular complexes with di-*n*-alkylamines. d) FTIR spectra of supramolecular complexes with *n*-alkylamines.

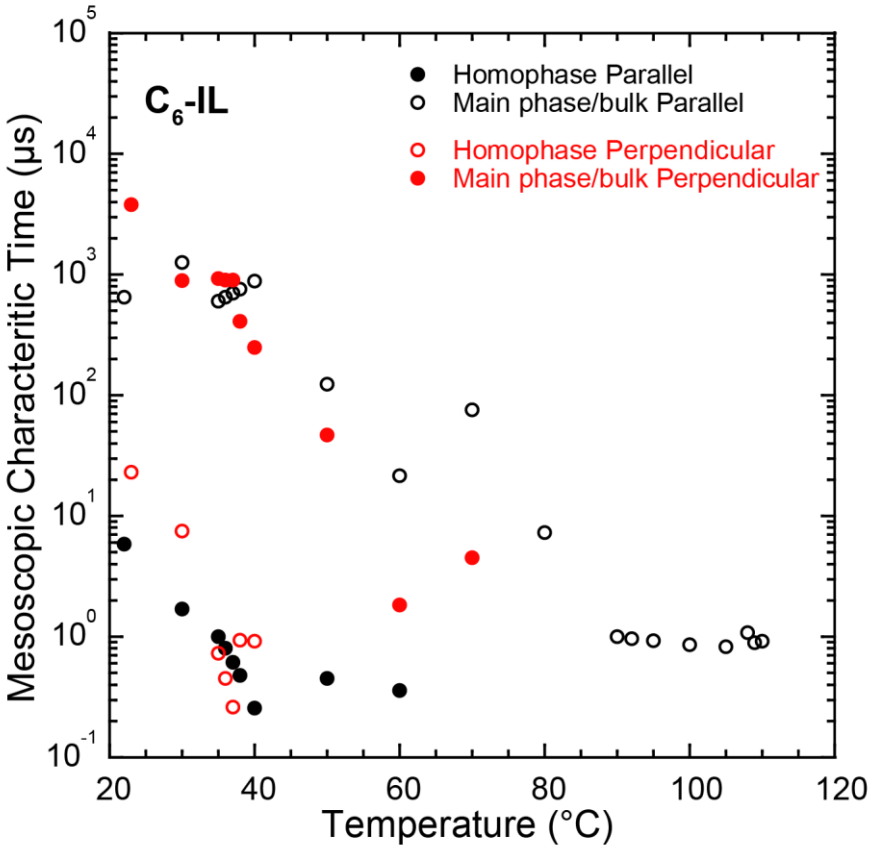

Figure S19. Temperature-dependent mesoscopic characteristic times for ion transport parallel and perpendicular to the ionic layers for the C_6-IL supramolecular complex. These times, not normalized by the respective volume fractions, show the transport anisotropy of the complex. Indeed, the measurements show two characteristic times for each configuration *i.e. parallel* and *perpendicular*. There are attributed to the same phase in two average orientations, *i.e.* in the main probed direction (main/bulk phase) and in the average of the other directions (the so-called homophase to describe separate regions of the same phase). As shown by the symmetry of the time evolutions, by changing the configuration, the observations are inversed/symmetrical. The main phase becomes the homophase (*i.e.* along the average of the other directions) and the homophase becomes the main phase (*i.e.* along the main probed direction). The characteristic times are low at high temperatures. This fast dynamics at the mesoscopic (*ca.* µm) scale should lead to high ionic conductivities but the lack of long-range structural order within C_6-IL prohibits the fast ionic transport.

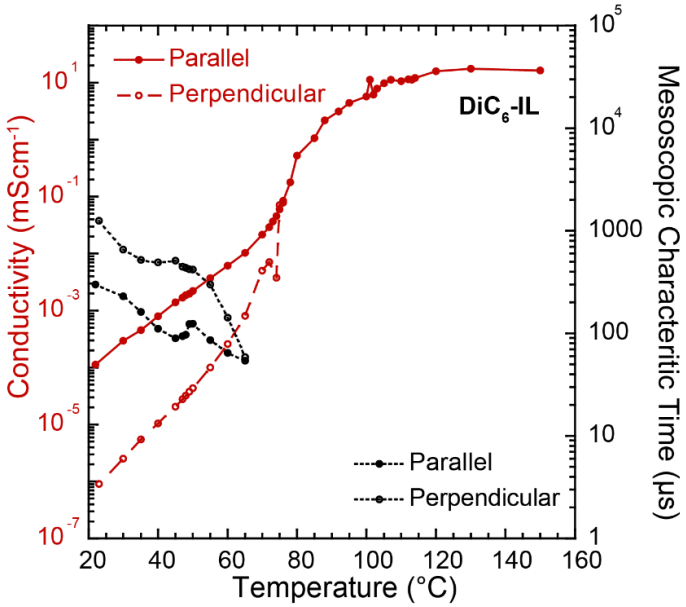

Figure S20. Temperature-dependent ionic conductivity and mesoscopic characteristic times in both parallel and perpendicular to ionic layers for the DiC_6-IL supramolecular complex. These times and conductivities indicate the anisotropy of the complex. These characteristic times are very low. This fast dynamics at the mesoscopic (*ca.* µm) scale should lead to high ionic conductivities but the lack of long-range structural order (see Figure S12e) within DiC_6-IL prohibit fast ionic transport.

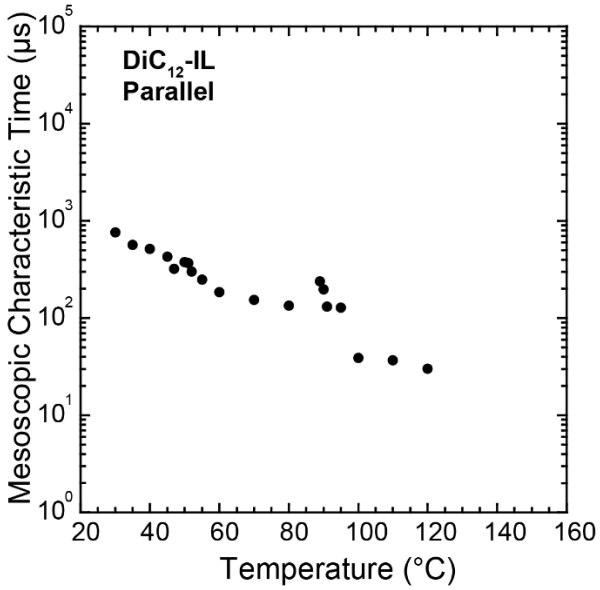

Figure S21. The suggested temperature dependent mesoscopic characteristic times for ion transport parallel to the ionic layers for the DiC_{12}-IL supramolecular complex.

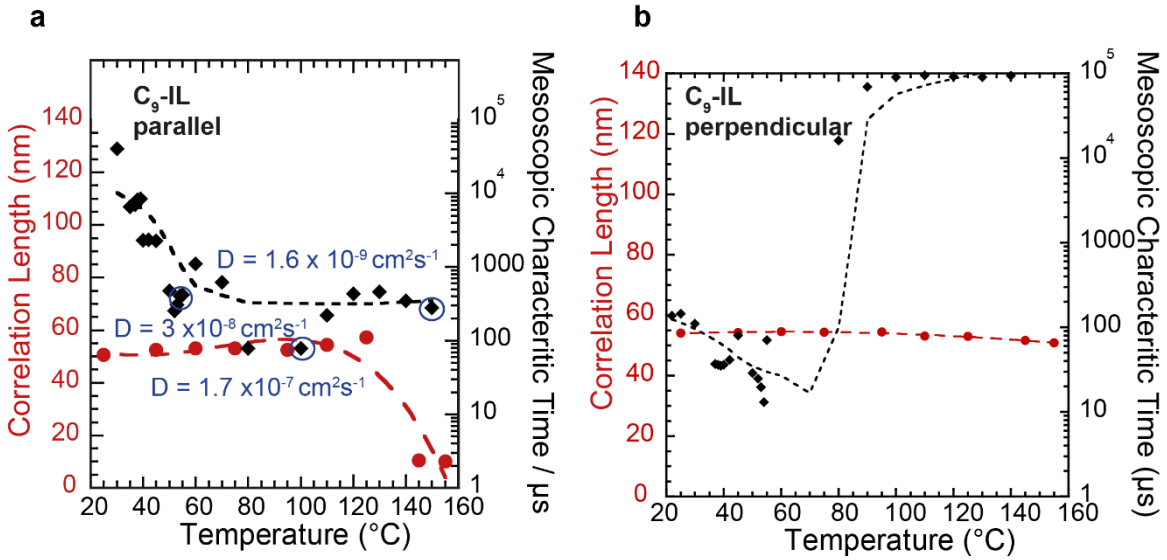

Figure S22. Temperature-dependent correlation lengths of the periodicities and corresponding characteristic times of ion transport for the C_9-IL supramolecular complex. a) The suggested correlation lengths parallel to the ionic layers and the corresponding characteristic times of the ion transport. b) The suggested correlation length perpendicular to the ionic layers and the corresponding characteristic times of the ion transport. The characteristic times for C_9-IL at elevated temperatures in both directions parallel and perpendicular to the ionic layers are notably larger than for the DiC_9-IL supramolecular complex, in addition with lower diffusion constants and correlation lengths.

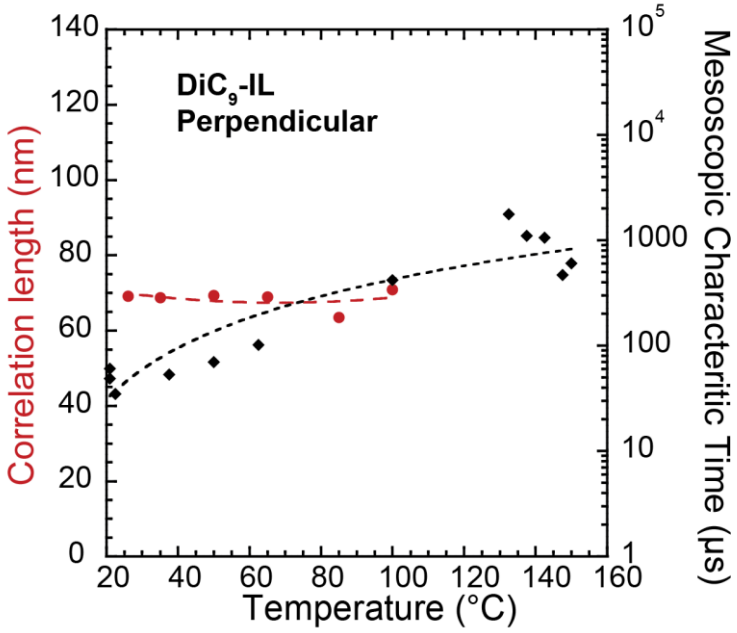

Figure S23. Temperature-dependent correlation lengths of the periodicity and characteristic times of the ion transport perpendicular (along the a-axis) to the ionic layers for the DiC_9-IL supramolecular complex.

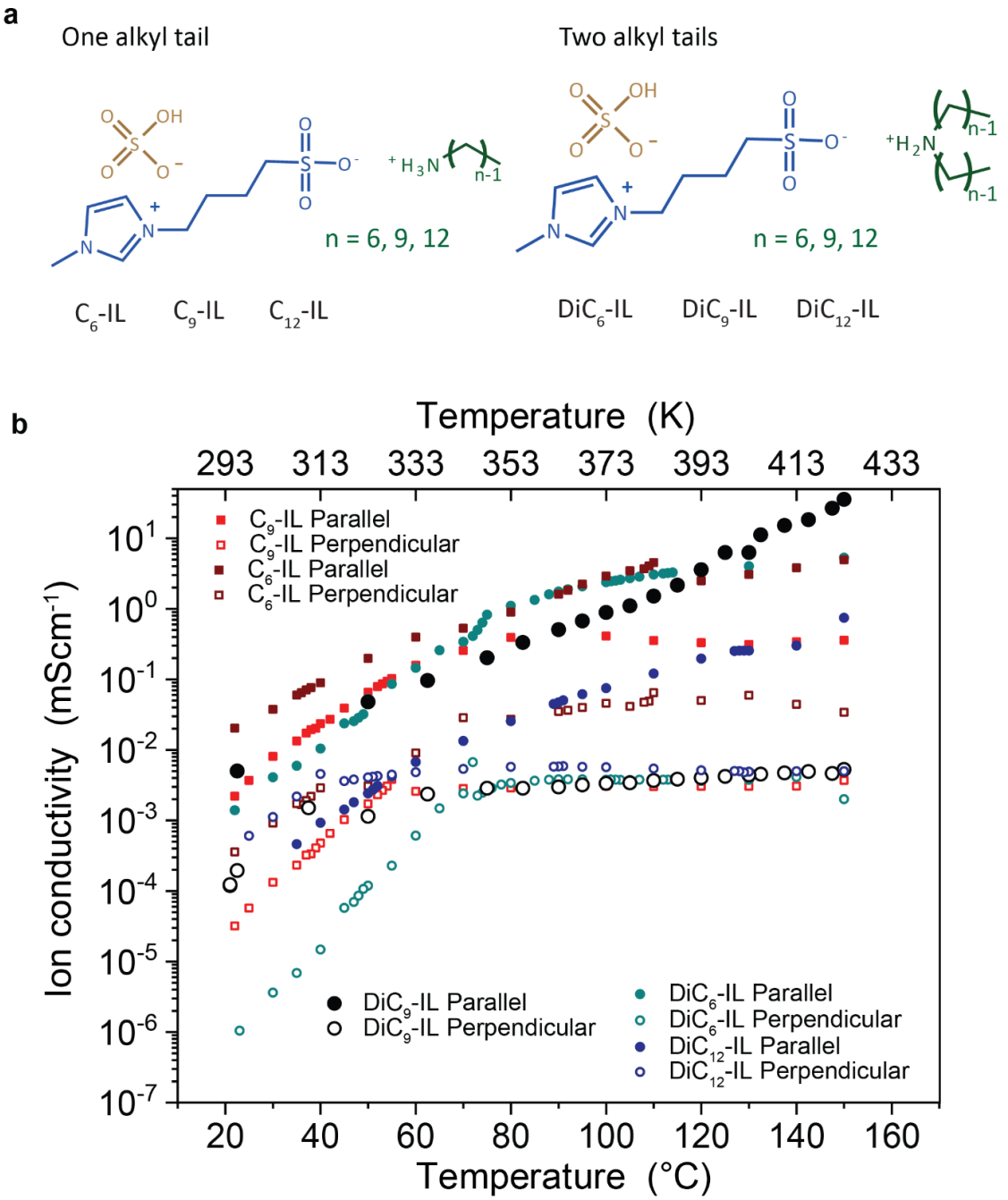

Figure S24. Temperature dependent parallel *vs.* perpendicular ionic conductivities for the family of surfactant self-assembled ionic liquid crystals. a) Chemical structures of the *n*-alkyl tail and di-*n*-alkyl tails surfactant-self-assembled C_x-IL and DiC_x-IL supramolecular complexes with (4-sulfobutyl)-3-methylimidazolium hydrogen sulfate. b) Parallel (*vs.* the ionic layers) and perpendicular (*vs.* the ionic layers) ionic conductivity of all surfactant self-assembled ionic liquid crystals as a function of temperature. All samples were characterized by EIS during cooling scans using a slow 0.5 °C·min^{-1} scanning rate. The kink in ion transport at lower temperatures is associated to *n*-alkyl or di-*n*-alkyl chain crystallizations, in agreement with DSC traces, leading to reduced electrical contact to the electrodes.

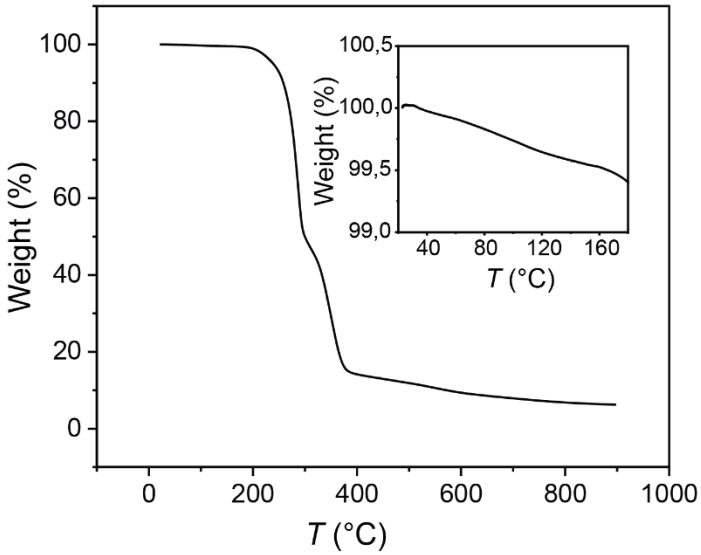

Figure S25. TGA of the DiC_9-IL supramolecular complex. TGA was measured using the rate of 10 °C·min^{-1} using nitrogen as the carrier gas. First, a gradual and small weight loss (<1 wt.%) is observed up to *ca*. 200 °C, attributed to water loss. Beyond *ca.* 200 °C, it is followed by a rapid and massive (> 90 wt.%) weight loss, reflecting the chemical degradation of the supramolecular complex at this high scan rate.

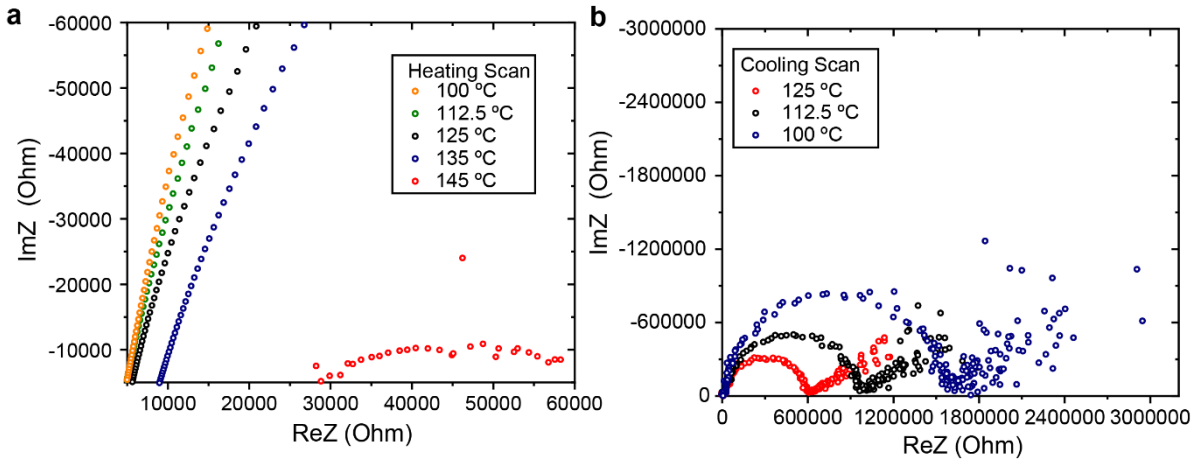

Figure S26. Irreversible chemical side reaction at the ITO electrodes by the uncomplexed acidic (4-sulfobutyl)-3-methylimidazolium hydrogen sulfate (IL) at elevated temperatures**.** a) Development of a broad, depressed semicircle in Nyquist plot at 145 °C during the heating scan of pure IL. This indicates chemical side reaction caused by the sulfonic acid end group of the IL on the ITO electrodes leading to formation of a resistive layer at their surfaces. b) Increase in size of the semicircle during EIS measurements performed during a cooling scan. Impedance diagrams recorded at the same temperature look different for heating and cooling scans, indicating that the electrodes have been irreversibly modified during the heating scan.

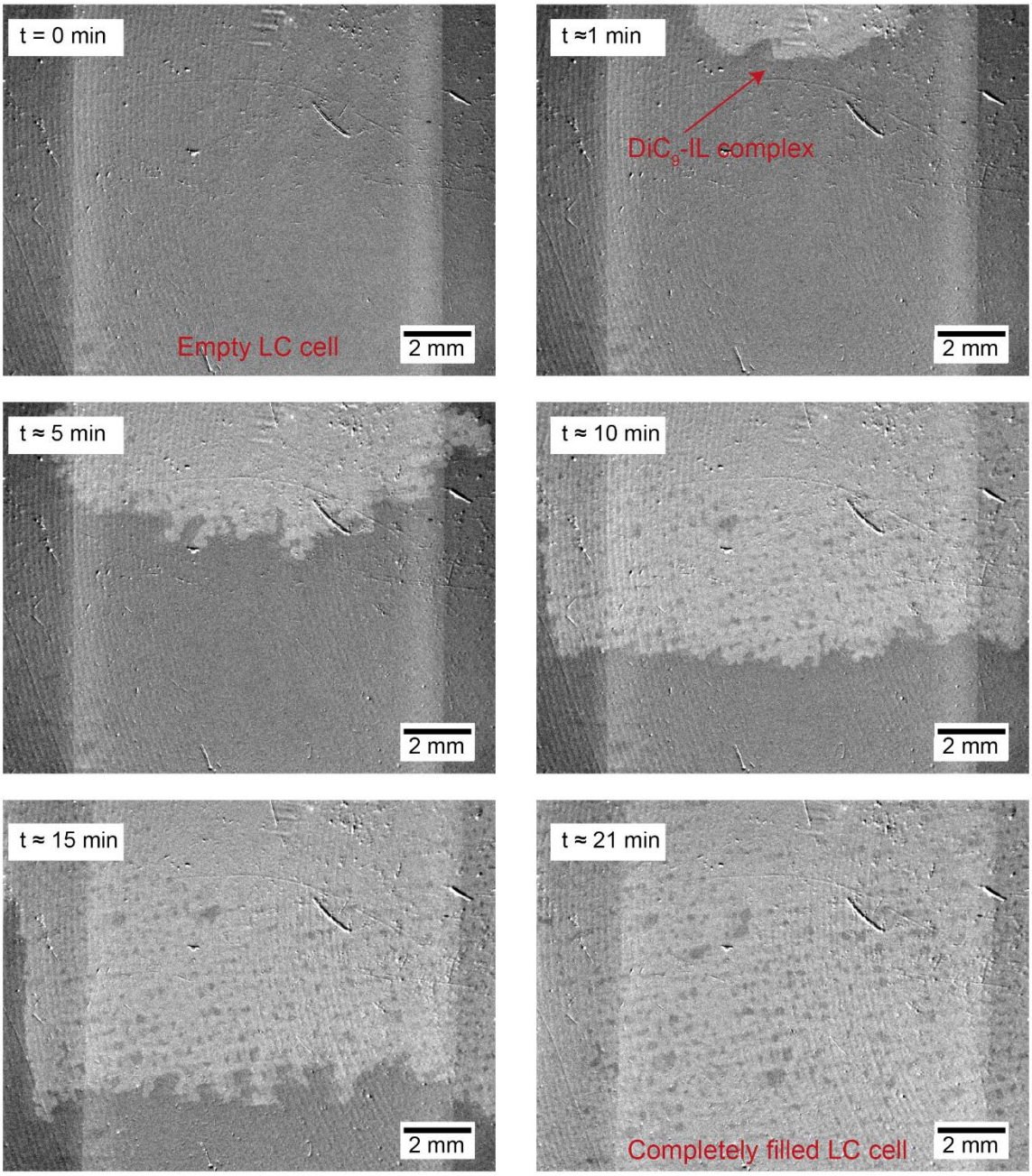

Figure S27. Optical images at different times showing the propagating front of the fluid mesophase of the DiC_9-IL supramolecular complex at 150 °C diffusing into the parallel slits between two glass slits by capillary action. This shows the fluid character of DiC_9-IL even if it shows the 2D crystalline reflections due to the 2D ionic crystalline sheets.

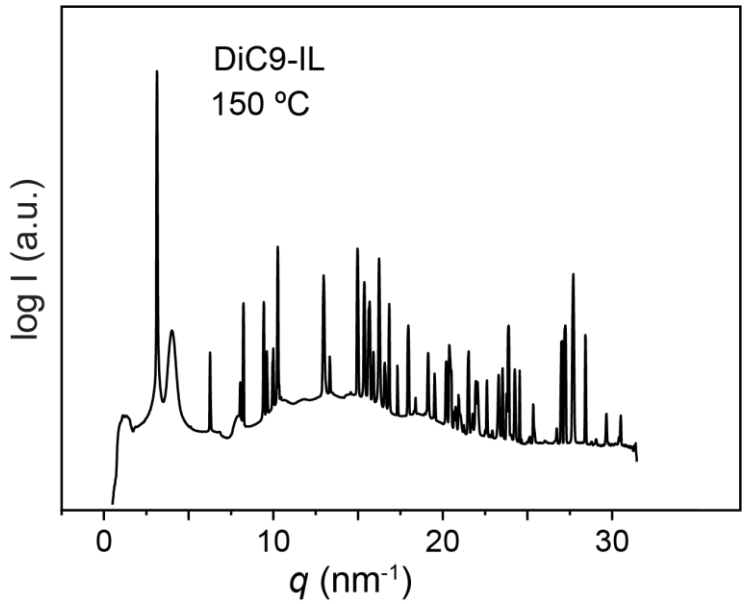

Figure S28. Close-up of the X-ray scattering patterns of DiC_9-IL supramolecular complex at 150 °C showing the amorphous halo due to the molten di-*n*-nonyl surfactant tails.

Supporting References

[S1] R. Ahlrichs, M. Bär, M. Häser, H. Horn, C. Kölmel, *Chem. Phys. Lett.* **1989**, *162*, 165.

[S2] F. Weigend, M. Häser, *Theor. Chem. Acc.* **1997**, *97*, 331.

[S3] F. Weigend, M. Häser, H. Patzelt, R. Ahlrichs, *Chem. Phys. Lett.* **1998**, *294*, 143.

[S4] A. D. Becke, *Phys. Rev. A* **1988**, *38*, 3098.

[S5] C. Lee, W. Yang, R. G. Parr, *Phys. Rev. B* **1988**, *37*, 785.

[S6] S. Grimme, *J. Comput. Chem.* **2006**, *27*, 1787.

[S7] J. I. Langford, A. J. C. Wilson, *J. Appl. Crystallogr.* **1978**, *11*, 102.

[S8] G. Socrates, *Infrared and Raman Characteristic Group Frequencies: Tables and Charts*, John Wiley & Sons Ltd, Chichester, England **2001**.

[S9] J. T. S. Irvine, D. C. Sinclair, A. R. West, *Adv. Mater.* **1990**, *2*, 132.

[S10] J. P. Diard, P. Landaud, B. Le Gorrec, C. Montella, *J. Appl. Electrochem.* **1992**, *22*, 1180.

[S11] M. Gellert, K. I. Gries, C. Yada, F. Rosciano, K. Volz, B. Roling, *J. Phys. Chem. C* **2012**, *116*, 22675.

[S12] S. K. Deraman, N. S. Mohamed, R. H. Y. Subban, *Int. J. Electrochem. Sci.* **2013**, *8*, 1459.

[S13] T. Kato, M. Yoshio, T. Ichikawa, B. Soberats, H. Ohno, M. Funahashi, *Nat. Rev. Mater.* **2017**, *2*, 17001.